Article

Artificial intelligence-enabled clinical phenotyping of human brown fat

https://doi.org/10.1038/s41586-026-11162-7

Received: 20 October 2025

Accepted: 14 September 2026

Published online: 14 October 2026

Open access

Check for updates

Nicolás Gómez-Banoy[1,2,3], Jorge A. Barrero[1,4], Luiza Rachel Pinheiro de Carvalho[1], Caroline S. Jiang[5], Tara Doma Lama[3,6], Nakul Karandikar[1,7], Mascha Koenen[1,8], Tiffany Lam[1,9], Kaja Plucińska[1], Ksenia Morozova[1], Stephanie Chahwan[10], Gustavo Barraza[10], Burcin Agridag Ucpinar[10], Jennifer E. Liu[11], Rohit Sharma[3,6], Daniel Lafontaine[12], Heiko Schöder[10] & Paul Cohen[1]✉

Adipose tissue has a central role in systemic energy balance and the pathogenesis of obesity and its sequelae[1,2]. In contrast to white adipose tissue, brown adipose tissue (BAT) uses energy to produce heat[3]. Detectable BAT in humans is associated with decreased prevalence of cardiometabolic diseases[4]. However, the complete spectrum of health conditions associated with BAT remains unknown, and high-throughput methods to quantify BAT activity in humans are lacking[5,6]. Here we leveraged big data and artificial intelligence to systematically define the clinical impact of BAT in a cohort of 101,243 patients from a large cancer centre. Our unbiased analyses revealed that, across all diagnoses, cardiovascular and psychiatric diseases were less prevalent in people with BAT. Using a machine learning approach, we semi-automatically quantified BAT activity in approximately 8,700 patients and demonstrated that higher BAT activity, especially in the axillary depot, is associated with lower odds of cardiometabolic diseases and healthier white fat distribution. People with BAT also exhibited more favourable glycaemic parameters, lipid profiles, inflammatory markers and echocardiographic indices. Analysis of medication usage demonstrated that angiotensin receptor blocker use was positively associated with BAT presence. As proof of concept, we showed that the angiotensin receptor blocker losartan increased brown adipocyte activity and whole-body energy expenditure. Altogether, our studies harnessing artificial intelligence and big data identify new clinical phenotypes linked to BAT and serve as a platform for drug repurposing to activate this tissue in humans.

Obesity is a major risk factor for type 2 diabetes (T2D), hypertension and cardiovascular disease[2,7]. Adipose tissue dysfunction is a hallmark of obesity and contributes to the pathophysiology of cardiometabolic diseases[1]. White adipose tissue (WAT) stores energy as triglyceride[1] in subcutaneous and visceral depots, and visceral adiposity is a key feature of metabolically unhealthy obesity[8]. By contrast, brown adipose tissue (BAT) dissipates energy as heat (thermogenesis) and its activation in animal models protects against obesity and metabolic diseases[3]. However, the relevance of BAT to adult human physiology and whether it can be targeted therapeutically remain unclear[5,6].

Since the landmark reports that adult humans have inducible BAT[9–12], several clinical studies have aimed to recruit BAT through cold exposure or β-adrenergic agonists[13–17]. Although these interventions activate BAT and improve glucose homeostasis, their side effects and the small number of participants studied have limited their clinical impact[5]. More recently, our group described the largest reported cohort of people with BAT and demonstrated that the presence of BAT in ^{18}F-fluorodeoxyglucose (18F-FDG) positron emission tomography (PET)–computed tomography (CT) (18F-FDG-PET–CT) scans obtained for clinical purposes and without previous stimulation was associated with reduced prevalence of cardiometabolic disease[4]. A caveat from this work is that patients were characterized based on BAT presence or absence, rather than by quantitative BAT metabolic activity. Like WAT, human BAT is localized in distinct anatomic depots[18], but whether these depots uniquely affect health remains unknown. Moreover, most human BAT studies have focused on cardiometabolic

[1]Laboratory of Molecular Metabolism, The Rockefeller University, New York, NY, USA. [2]Department of Medicine, Division of Endocrinology, Memorial Sloan Kettering Cancer Center, New York, NY, USA. [3]Department of Medicine, Division of Endocrinology, Diabetes and Metabolism, Weill Cornell Medicine, New York, NY, USA. [4]Departamento de Ciencias Fisiológicas, Laboratorio de Lípidos y Diabetes, Facultad de Medicina, Universidad Nacional de Colombia, Bogota, Colombia. [5]Center for Clinical and Translational Science, The Rockefeller University, New York, NY, USA. [6]Metabolic Phenotyping Center, Core Laboratories Center, Weill Cornell Medicine, New York, NY, USA. [7]Weill Cornell/Rockefeller/Sloan Kettering Tri-Institutional MD-PhD Program, New York, NY, USA. [8]Laboratory of Tissue Dynamics and Organ Crosstalk, Helmholtz Institute for Translational AngioCardioScience (HI-TAC) of the Max Delbrück Center for Molecular Medicine in the Helmholtz Association at Heidelberg University, Mannheim, Germany. [9]Department of Medicine, Weill Cornell Medicine/New York Presbyterian Hospital, New York, NY, USA. [10]Department of Radiology, Memorial Sloan Kettering Cancer Center, New York, NY, USA. [11]Department of Medicine, Cardiology Service, Memorial Sloan Kettering Cancer Center/Weill Cornell Medicine, New York, NY, USA. [12]Department of Medical Physics, Memorial Sloan Kettering Cancer Center, New York, NY, USA. ✉e-mail: pcohen@rockefeller.edu

outcomes, but how this tissue influences other organ systems and disease types remains largely unexplored. These limitations have hindered the identification of pharmacologic agents that promote BAT activity, and there are no approved, widely used medications to leverage the cardiometabolic benefits linked to this tissue.

In this study we expanded our cohort to more than 100,000 patients and performed an unbiased, comprehensive analysis across all diagnostic codes to identify new clinical phenotypes linked to BAT presence. Furthermore, we harnessed artificial intelligence (AI) to semi-automatically quantify total and depot-specific BAT metabolic activity from 18F-FDG-PET–CT scans. This allowed us to investigate associations between specific BAT depots, WAT distribution and cardiometabolic outcomes. Finally, we combined these approaches with medication use analyses to identify pharmacologic regulators of BAT and performed proof-of-concept experiments to validate losartan as an activator of brown adipocytes through a unique, peroxisome proliferator-activated receptor-γ (PPARγ)-dependent mechanism.

Associations of BAT with all diagnoses

To discover associations between BAT and diseases beyond the cardiometabolic system, we expanded our previously described cohort (Established BAT Cohort)[4] by reviewing additional FDG-PET–CT scans taken from 2018 to 2024 at Memorial Sloan Kettering Cancer Center. Of these, 4.4% reported BAT presence and 4,778 patients (7.9%) had at least one scan positive for BAT (hereafter termed BAT positive (BAT^+); Extended Data Fig. 1a). The remaining patients were designated BAT negative (BAT^-). These newly identified participants were grouped in an Extension BAT Cohort (Extended Data Fig. 1a) that validated findings from our Established BAT Cohort[4] demonstrating lower prevalence of cardiometabolic diseases in people who are BAT^+ (Extended Data Fig. 1b). To increase statistical power, we merged the Established and Extension BAT Cohorts to create an Expanded BAT Cohort, consisting of 101,243 patients, of whom 8,897 were BAT^+ and 92,346 were BAT^-. Each patient was assigned an index scan as a reference point for clinical data collection (Extended Data Fig. 1a). Similar to previous findings[4], BAT was more prevalent in women in the Expanded BAT Cohort, and its prevalence decreased with age, higher ambient temperature at the time of the scan and increasing body mass index (BMI) (Extended Data Fig. 1c–f).

Given the influence of these variables on BAT prevalence, we used propensity score matching (PSM) to create a cohort of patients in the BAT^+ ($n = 8,897$) and BAT^- ($n = 17,405$) groups balanced across age, sex, BMI and ambient temperature (Extended Data Fig. 1g,h). As patients in our cohort come from a cancer centre, we extracted extensive cancer-associated data (Supplementary Tables 1 and 2) for each patient in our PSM cohort, including site, stage and treatment. We confirmed that certain cancer sites were more frequent (for example, breast and oral cavity), less frequent (for example, digestive) or had no association (for example, skin, urinary) with BAT presence (Table 1). As in our previous report, some cancer treatments were used more frequently in the BAT^+ group[4] (Table 1). Consequently, all cancer-associated variables were controlled for unless otherwise stated for the remainder of this study. We then performed multi-variable logistic regression in this new, expanded PSM cohort and confirmed the association between BAT presence and decreased prevalence of select cardiometabolic diseases[4] (Extended Data Fig. 1i). Given the sexual dimorphism in BAT presence and cardiometabolic traits, we performed separate analyses in women and men and found that BAT was associated with decreased odds of cardiometabolic diseases in both sexes in our PSM and Extension BAT Cohorts (Extended Data Fig. 2a,b).

Next, we used an unbiased approach to establish associations between BAT and diseases across all organ systems in our PSM cohort (Fig. 1a). After extraction of International Classification of Diseases (ICD) code data and initial screening analysis (Fig. 1a), 104 of 511 codes exhibited significant, non-adjusted associations with BAT (Supplementary Table 3). Over-representation analysis revealed that cardiovascular and psychiatric diagnoses were enriched significantly in their association with BAT (Fig. 1b). We then ran a multi-variable logistic regression for each of the 104 codes to establish associations with BAT, adjusting for multiple co-variates. This resulted in 98 codes that were significant after adjustment, with 92 showing lower incidence in patients in the BAT^+ group (Fig. 1a and Supplementary Table 4).

Among the top 20 codes with lower prevalence in the BAT^+ group, the two most significant were T2D (odds ratio (OR) 0.42; 95% confidence interval (CI) 0.35–0.50; $P < 0.001$) and chronic ischaemic heart disease (OR 0.53; 95% CI 0.44–0.62; $P < 0.001$); other cardiometabolic codes such as disorders of lipoprotein metabolism (OR 0.76; 95% CI 0.70–0.83; $P < 0.001$) and primary hypertension (OR 0.79; 95% CI 0.73–0.85; $P < 0.001$) were also present. We also identified associations with other disease systems, including decreased odds of respiratory failure (OR 0.46; 95% CI 0.37–0.57; $P < 0.001$), ascites (OR 0.51; 95% CI 0.43–0.62; $P < 0.001$), anxiety disorders (OR 0.78; 95% CI 0.73–0.84; $P < 0.001$), depressive episode (OR 0.68; 95% CI 0.61–0.76; $P < 0.001$) and sleep disorders (OR 0.77; 95% CI 0.71–0.85; $P < 0.001$) in patients who were BAT^+ (Fig. 1c). Among codes with higher prevalence in the BAT^+ group, five of six were skin diagnoses (Extended Data Fig. 2c). BAT^+ status also trended toward being associated with a higher prevalence of osteoporosis, although this did not reach statistical significance in the adjusted analysis (Extended Data Fig. 2c).

AI-enabled BAT activity and clinical links

We used a newly developed machine learning-based approach (TriDFusion (3DF))[19] to semi-automatically measure total and depot-specific BAT metabolic activity (defined as product of the mean standard 18F-FDG uptake value (standardized uptake value (SUV)) and BAT volume in millilitres) from most patients with BAT^+ status ($n = 8,709$; 97.9% of the BAT^+ group (Methods)) in our Expanded BAT Cohort (Fig. 2a,b). Among the six previously described BAT depots, the supraclavicular had the highest prevalence and activity (Extended Data Fig. 3a,b). Total BAT metabolic activity was correlated inversely with age and was higher in women (Extended Data Fig. 3c–f). As cardiometabolic diagnoses exhibited the strongest link with BAT (Fig. 1b), we stratified our 8,709 patients with BAT activity measurements into tertiles and examined whether increasing total and depot-specific BAT activity was associated with decreased odds of cardiometabolic diseases using patients in the BAT^- group as a reference. Indeed, higher total BAT metabolic activity was associated with a stepwise reduction in the prevalence of T2D ($P < 0.001$), atrial fibrillation and/or atrial flutter ($P < 0.001$), coronary artery disease (CAD; $P < 0.001$) and congestive heart failure ($P < 0.001$), even after controlling for age, BMI, sex and outside temperature (Fig. 2c).

BAT in humans is localized in several depots, which could have distinct functions depending on their location or could contain different cell types[20–22]. Until now, it was not feasible to perform large-scale analyses with depot-level resolution, so we used our AI tool to compare the association between cardiometabolic diagnoses and BAT metabolic activity in each of the six different BAT depots compared with patients in the BAT^- group (Fig. 2c). Within the most prevalent depot, the supraclavicular, increasing BAT activity was associated with clear, dose-dependent reduced odds of T2D ($P < 0.001$) and CAD ($P < 0.001$) in all tertiles. In both the cervical and supraclavicular depots, higher BAT activity was associated with lower odds of hypertension, but this effect was lost for patients with highest BAT activity (tertile 3) (Fig. 2c). Of note, increasing axillary BAT activity was associated with significant reductions in the prevalence of all cardiometabolic diseases queried (including cerebrovascular disease), with a clear stepwise decrease in the risk of hypertension, in contrast to most other depots (Fig. 2c).

We carried out similarly controlled analyses within patients with BAT^+ status, using patients in tertile 1 as a reference. Given the low prevalence

Table 1 | Demographic and clinical characteristics of patients in the BAT$^+$ and BAT$^-$ groups from the PSM cohort

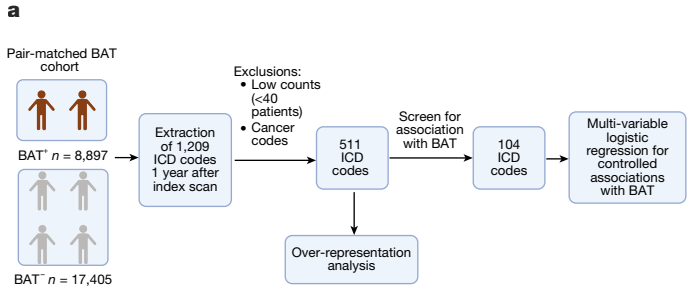
Characteristic	BAT$^-$ (n=17,405)	BAT$^+$ (n=8,897)	Pvalue[a]
Mean age (years)	50.9±15.0	50.0±16.7	<0.001
Sex (n (%))			0.16
Female	13,548 (77.8)	6,856 (77.1)	
Male	3,857 (22.2)	2,041 (22.9)	
Mean BMI (kg m^{-2})	25.9±5.6	25.9±5.5	0.55
BMI category (n (%))			
<25.0	8,826 (49.6)	4,446 (50.0)	0.53
25.0–29.9	5,279 (30.3)	2,788 (31.3)	0.13
≥30.0	3,500 (20.1)	1,663 (18.7)	0.01
Ethnicity (n (%))[b]			
Hispanic	1,372 (7.9)	817 (9.2)	<0.001
Non-Hispanic	15,049 (86.5)	7,583 (85.2)	0.006
Unknown	984 (5.6)	497 (5.6)	0.82
Race (n (%))[b]			
Asian	1,685 (9.7)	863 (9.7)	0.96
African American	1,548 (8.9)	1,094 (12.3)	<0.001
Caucasian	12,821 (73.7)	6,107 (68.6)	<0.001
Other and/or unknown	1,351 (7.8)	833 (9.4)	<0.001
Ambient temperature at index ^{18}FDG-PET–CT scan (°C)	12.2±8.5	12.2±8.3	0.78
Cancer site (n (%))			
Bones, joints and/or cartilage	254 (1.5)	174 (2.0)	0.003
Breast and/or female genitalia	5,653 (32.5)	3,121 (35.1)	<0.001
Digestive	2,002 (11.5)	725 (8.1)	<0.001
Eye, brain and/or central nervous system	238 (1.4)	83 (1.0)	0.002
Haematopoietic and/or reticuloendothelial	856 (4.9)	344 (3.9)	<0.001
Lip, oral and/or pharynx	859 (4.9)	565 (6.3)	<0.001
Male genitalia	307 (1.8)	189 (2.1)	0.04
Peripheral autonomic nervous system, and/or retroperitoneal and peritoneal tissues	376 (2.2)	239 (2.7)	0.008
Intrathoracic and/or respiratory	2,194 (12.6)	1,042 (11.7)	0.04
Skin	668 (3.8)	330 (3.7)	0.60
Thyroid and/or other endocrine cancer	555 (3.2)	299 (3.4)	0.46
Urinary	330 (1.9)	172 (1.9)	0.83
Unknown origin	2,121 (12.2)	1,299 (14.6)	<0.001
Not applicable	992 (5.7)	315 (3.5)	<0.001
Cancer treatment (n (%))			
Radiation therapy	599 (3.4)	500 (5.6)	<0.001
Immunomodulatory therapy	909 (5.2)	639 (7.2)	<0.001
Mitotic inhibitor	1,473 (8.5)	1,251 (14.1)	<0.001
Targeted therapy	712 (4.1)	577 (6.5)	<0.001
Kinase inhibitor	213 (1.2)	128 (1.4)	0.15
Hormonal therapy	495 (2.8)	403 (4.5)	<0.001
Alkylating agent	1,734 (10.0)	1,287 (14.5)	<0.001
Antimetabolite	1,087 (6.2)	599 (6.7)	0.13
Cancer antibiotic	738 (4.2)	672 (7.5)	<0.001
Other	383 (2.2)	221 (2.5)	0.15

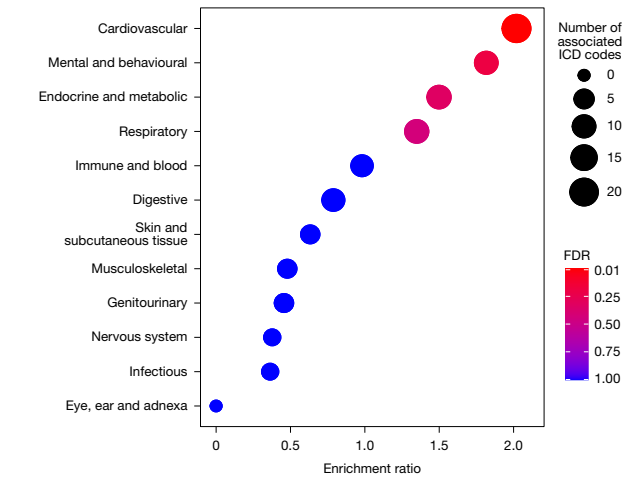
Data are from a PSM cohort based on age, sex, BMI and ambient temperature at the time of index scan. Values are means±s.d. unless otherwise stated.

[a]P values were calculated for continuous variables using an unpaired two-tailed t-test, with variance equality assessed using an F-test of sample variances. When variances were equal, standard t-tests assuming equal variances were used; otherwise, t-tests with unequal variance adjustments were applied. For categorical variables, frequencies were compared using chi-square tests.

[b]Race and ethnicity were self-reported and collected from the institutional electronic health records (EHRs).

of cardiometabolic disease in people with BAT, the associations were not as statistically powerful, but we identified similar trends (Extended Data Fig. 3g). Increasing total BAT metabolic activity was associated with lower odds of T2D (P = 0.009) and CAD (P = 0.03) in this analysis. Within the cervical depot, higher BAT activity was associated with a slight reduction in the incidence of CAD (P = 0.04), but increased odds





c

Diagnosis (ICD code)	BAT⁻ No. of patients with diagnosis/total no. of patients (%)	BAT⁺ No. of patients with diagnosis/total no. of patients (%)	OR (95% CI)	Adjusted *P* value
Type 2 diabetes (E11)	884/17,405 (5.1)	184/8,897 (2.1)	0.42 (0.35–0.50)	<0.001
Chronic ischaemic heart disease (I25)	718/17,405 (4.1)	209/8,897 (2.3)	0.53 (0.44–0.62)	<0.001
Respiratory failure not elsewhere classified (J96)	467/17,405 (2.7)	123/8,897 (1.4)	0.46 (0.37–0.57)	<0.001
Ascites (R18)	603/17,405 (3.5)	168/8,897 (1.9)	0.51 (0.43–0.62)	<0.001
Unspecified diabetes mellitus (E14)	485/17,405 (2.8)	112/8,897 (1.3)	0.47 (0.38–0.58)	<0.001
Other functional intestinal disorders (K59)	4,377/17,405 (25.1)	1,982/8,897 (22.3)	0.80 (0.75–0.85)	<0.001
Other anxiety disorders (F41)	3,414/17,405 (19.6)	1,438/8,897 (16.2)	0.78 (0.73–0.84)	<0.001
Depressive episode (F32)	1,421/17,405 (8.2)	484/8,897 (5.4)	0.68 (0.61–0.76)	<0.001
Disorders of lipoprotein metabolism (E78)	3,210/17,405 (18.4)	1,324/8,897 (14.9)	0.76 (0.70 – 0.83)	<0.001
Dorsalgia (M54)	1,965/17,405 (11.3)	828/8,897 (9.3)	0.74 (0.67–0.81)	<0.001
Nausea and vomiting (R11)	3,433/17,405 (19.7)	1,543/8,897 (17.3)	0.79 (0.74–0.85)	<0.001
Other disorders of fluid and electrolytes (E87)	2,678/17,405 (15.4)	1,135/8,897 (12.8)	0.77 (0.71–0.83)	<0.001
Essential primary hypertension (I10)	4,142/17,405 (23.8)	1,839/8,897 (20.7)	0.79 (0.73–0.85)	<0.001
Pleural effusion not elsewhere classified (J90)	1,533/17,405 (8.8)	585/8,897 (6.6)	0.71 (0.64–0.79)	<0.001
Disorders of mineral metabolism (E83)	1,982/17,405 (11.4)	845/8,897 (9.5)	0.76 (0.70–0.83)	<0.001
Malaise and fatigue (R53)	2,545/17,405 (14.6)	1,137/8,897 (12.8)	0.80 (0.74–0.87)	<0.001
Sleep disorders (G47)	1,882/17,405 (10.8)	782/8,897 (8.8)	0.77 (0.71–0.85)	<0.001
Lack of expected normal physiological development (R62)	391/17,405 (2.2)	124/8,897 (1.4)	0.55 (0.45–0.69)	<0.001
Pneumonia due to organism (J18)	792/17,405 (4.6)	288/8,897 (3.2)	0.67 (0.58–0.78)	<0.001
Reaction to severe stress (F43)	1,276/17,405 (7.3)	480/8,897 (5.4)	0.74 (0.66–0.82)	<0.001

Fig. 1 | Associations of BAT with clinical diagnoses. a, Strategy for unbiased identification of diagnostic codes linked with BAT in our PSM cohort. **b**, Over-representation analysis of the association between 511 ICD codes grouped by system and BAT status. Statistical significance of over-representation was assessed using Fisher's exact test, and Benjamini–Hochberg false discovery rate (FDR) was used for multiple test adjustments. **c**, Forest plot of ORs for the most significant associations between diagnoses with lower prevalence in patients in the BAT⁺ group (sorted by *P* value). Blue circle, estimated OR; error bars, corresponding 95% CI. The ORs and *P* values were obtained using multivariable logistic regression after adjustment for age, sex, BMI, ambient temperature, self-reported race and ethnicity, smoking history, family history of cardiovascular disease, cancer site, cancer stage, cancer treatment and general groups of outpatient medications. Panel **a** created in BioRender; Cohen, P. https://biorender.com/9utgkt8 (2026).

of hypertension ($P < 0.001$). Increasing mediastinal BAT activity was associated exclusively with reduced CAD prevalence ($P = 0.004$)—an interesting finding given its anatomical location. Of note, higher axillary BAT activity also showed the greatest effects in this analysis, associating with reductions in T2D ($P = 0.03$), congestive heart failure ($P = 0.02$) and hypertension ($P = 0.005$) (Extended Data Fig. 3g).

Given the well described association between WAT distribution and cardiometabolic disease[8], we used the CT portion of each 18F-FDG-PET–CT scan to semi-automatically measure the subcutaneous adipose tissue (SAT) and visceral adipose tissue (VAT) area. We were able to obtain these measurements and the SAT to VAT ratio in 8,040 patients in the BAT⁺ group (92.3% of patients with BAT from our PSM cohort; Extended Data Fig. 4a). We then performed linear regression analyses between BAT activity and WAT distribution parameters. From here on, most variables were log transformed due to non-normal data distribution and, consequently, coefficients (β) derived from the linear regression appear numerically small, as they reflect proportional relationships rather than raw changes. Total BAT metabolic activity showed a positive association with SAT area ($P < 0.001$), negative association with VAT area ($P < 0.001$) and positive association with SAT to VAT ratio (Fig. 2d,e). Given our previous findings, we assessed the association between depot-specific BAT activity and WAT distribution. Supraclavicular (Extended Data Fig. 4b,c), mediastinal (Extended Data Fig. 4f,g) and abdominal (Extended Data Fig. 4j,k) BAT metabolic activity behaved similarly to total BAT, exhibiting positive associations with SAT area and SAT to VAT ratio, and negative associations with VAT area. Paraspinal (Extended Data Fig. 4h,i) and cervical (Extended Data Fig. 4d,e) BAT (the latter exhibiting an association with increased odds of hypertension) were associated positively with SAT and VAT. Finally, axillary BAT (Fig. 2f,g), which was associated most strongly with decreased odds of cardiometabolic diseases, exhibited the most significant negative association with VAT area and, consequently, the strongest positive association with SAT to VAT ratio. Collectively, these data highlight the unique phenotypes linked to different BAT depots.

BAT activity and diagnostic studies

To further investigate clinical correlates of BAT we extracted an expanded battery of available laboratory tests and imaging studies from patients in our PSM cohort (Extended Data Fig. 5a) and performed analyses to identify differences between patients in the BAT⁺ and BAT⁻ groups (Supplementary Table 5). Patients with BAT had lower glucose ($P < 0.001$), haemoglobin A1C (HbA1c) ($P < 0.001$), triglycerides ($P < 0.001$) and triglyceride-glucose index, as well as higher high-density lipoprotein (HDL) cholesterol (HDL-C) levels ($P < 0.001$), even after adjusting for confounders (Fig. 3a and Extended Data Fig. 5b). Paradoxically, patients with BAT also had higher total cholesterol and low-density lipoprotein cholesterol (LDL-C). However, remnant cholesterol (total cholesterol − LDL − HDL)—an independent risk factor for atherosclerotic cardiovascular disease[23]—was significantly lower

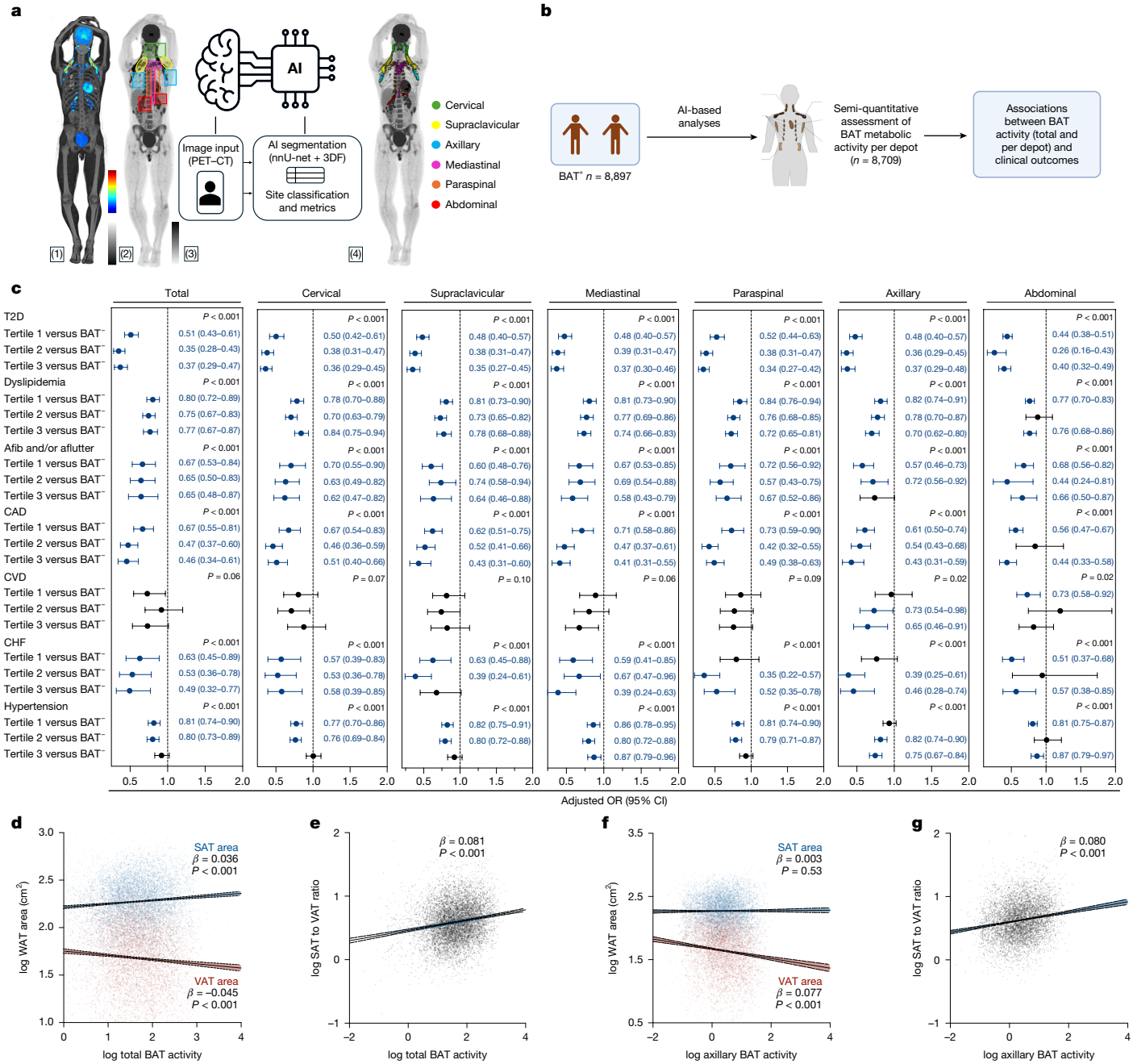


Fig. 2 | Assessment of BAT metabolic activity using AI and associations with cardiometabolic outcomes. a, Schematic of the 3DF BAT AI workflow: (1) three-dimensional (3D) volume rendering of CT image fused with 3D maximum intensity projection (MIP) of corresponding PET images. (2) 3D MIP of the PET image showing the different anatomical regions (in distinct colours) used as training sites for the AI model. (3) Diagram illustrating the 3DF nnU-net machine learning segmentation workflow. PET and CT images are processed by nnU-net to generate segmentation predictions. 3DF prepares the data for nnU-net, imports resulting predictions and exports metrics by anatomical site. (4) 3D MIP PET image fused with 3D volume-rendered nnU-net predictions, with each anatomical site depicted in distinct colours. **b**, Strategy for semi-automatic quantification of BAT metabolic activity in patients with BAT and proposed analyses. **c**, Forest plot of adjusted ORs for associations between total and depot-specific BAT activity stratified in tertiles ($n = 2,680$ per tertile) and cardiometabolic diseases using patients in the BAT⁻ ($n = 17,405$) group as a reference. Blue circle, estimated OR; error bars, corresponding 95% CI. The ORs and P values were obtained using multi-variable logistic regression analysis adjusted for age, sex, BMI and outdoor temperature. **d**,**e**, Scatter graphs depicting the association between total BAT metabolic activity and SAT and VAT area (**d**), and SAT to VAT ratio ($n = 8,040$) (**e**). **f**,**g**, Scatter graphs depicting association between axillary BAT metabolic activity and SAT and VAT area (**f**) or SAT to VAT ratio (**g**) ($n = 6,033$). Associations between BAT metabolic activity (expressed as the product of SUV and BAT volume in millilitres) and SAT area, VAT area and SAT to VAT ratio were calculated using linear regression after logarithmic transformation. Regression coefficients (β) and corresponding P values are reported. Afib, atrial fibrillation; Aflutter, atrial flutter; CHF, congestive heart failure. Panels **a** and **b** created in BioRender: **a**, Gómez-Banoy, N. https://biorender.com/wxfjd70 (2026); **b**, Gómez-Banoy, N. https://biorender.com/xuer3ef (2026).

in patients with BAT (Extended Data Fig. 5b). Finally, patients with BAT exhibited lower circulating brain natriuretic peptide (BNP) (Extended Data Fig. 5b).

To expand on these observations, we used semi-quantitative BAT data from our AI tool to establish associations between continuous clinical parameters and BAT activity. We found an inverse association

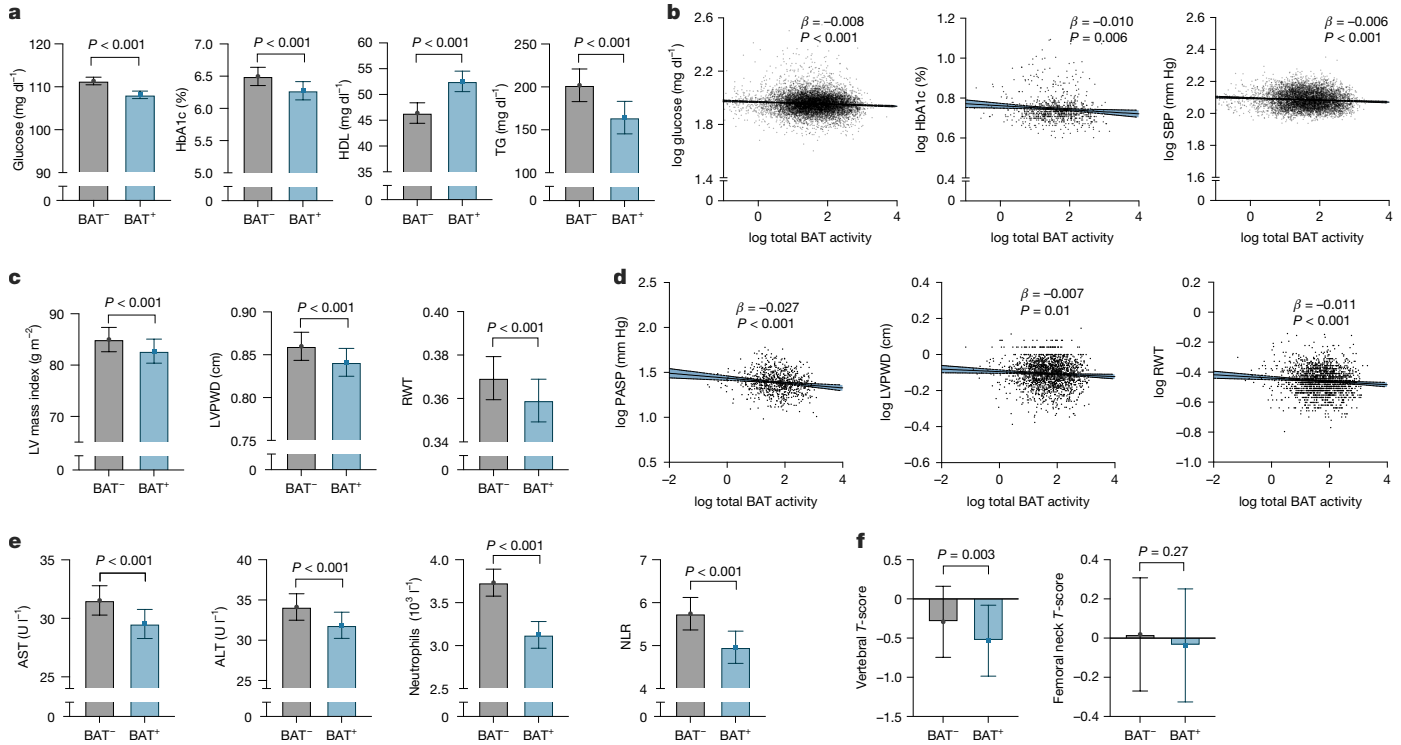


Fig. 3 | Associations of BAT presence and activity with laboratory values and diagnostic imaging. a, Comparisons of metabolic laboratory values in patients in the BAT$^-$ versus BAT$^+$ groups: glucose (BAT$^-$, n = 17,338; BAT$^+$, n = 8,877), HbA1c (BAT$^-$, n = 2,036; BAT$^+$, n = 841), HDL-C (BAT$^-$, n = 1,587; BAT$^+$, n = 828) and triglycerides (BAT$^-$, n = 1,996; BAT$^+$, n = 995). **b**, Association between total BAT metabolic activity and glucose (n = 8,709), HbA1c (n = 822) and systolic blood pressure (n = 6,482) values. **c**, Comparisons of echocardiographic measurements in patients in the BAT$^-$ versus BAT$^+$ groups: left ventricular mass index (BAT$^-$, n = 3,289; BAT$^+$, n = 1,733), LVPWD (BAT$^-$, n = 3,305; BAT$^+$, n = 1,743) and relative wall thickness (RWT) (BAT$^-$, n = 3,305; BAT$^+$, n = 1,743). **d**, Association between total BAT metabolic activity and PASP (n = 764), LVPWD (n = 1,711) and RWT (n = 1,711). **e**, Comparisons of hepatic and inflammatory laboratory values in patients in the BAT$^-$ versus BAT$^+$ groups: aspartate aminotransferase (BAT$^-$, n = 15,506; BAT$^+$, n = 8,078), alanine aminotransferase (BAT$^-$, n = 15,509; BAT$^+$, n = 8,082), neutrophil counts (BAT$^-$, n = 14,874; BAT$^+$, n = 7,827) and neutrophil-to-lymphocyte ratio (NLR) (BAT$^-$, n = 14,575; BAT$^+$, n = 7,670). **f**, Comparisons of DEXA scan measurements in patients in the BAT$^-$ versus BAT$^+$ groups: vertebral T-score (BAT$^-$, n = 911; BAT$^+$, n = 468) and femoral neck T-scores (BAT$^-$, n = 914; BAT$^+$, n = 470). In **a**,**c**,**e** and **f**, bar graphs depict mean values and error bars depict s.e.m. P values were obtained using a general linear model (GLM) followed by post hoc Tukey's honest significance difference (HSD) test to compare least square means, adjusted for age, sex, BMI, race, ethnicity, ambient temperature, cancer site and stage, cancer treatment and outpatient medications. In **b** and **d**, associations between BAT metabolic activity (expressed as the product of SUV and BAT volume in millilitres) and clinical continuous variables were calculated using linear regression after logarithmic transformation. Regression coefficients (β) and corresponding P values are reported. ALT, alanine aminotransferase; AST, aspartate aminotransferase; LV, left ventricular; SBP, systolic blood pressure; TG, triglycerides.

between total BAT metabolic activity and glucose levels (P < 0.001), HbA1c (P = 0.006), systolic blood pressure (P < 0.001) (Fig. 3b), mean arterial blood pressure (P < 0.001) and BNP (P = 0.01) and a trend with diastolic blood pressure (P = 0.12) (Extended Data Fig. 5c). We did not observe statistically significant associations between total BAT activity and lipids (Extended Data Fig. 5c).

Given the absence of large-scale studies linking BAT status with cardiac imaging in humans, and the association of BAT with higher carotid elasticity in a small prospective study[24], we extracted available echocardiogram data from patients in our PSM cohort and performed association analyses. In alignment with previous findings[25], patients with BAT had significantly lower left ventricular mass index (P < 0.001), left ventricular posterior wall thickness in diastole (LVPWD) (P < 0.001), relative wall thickness (P < 0.001) (Fig. 3c), pulmonary artery systolic pressure (PASP) and mitral valve E/e' ratio, with no changes in ejection fraction, left atrial volume index and mitral valve E/A ratio (Extended Data Fig. 5d). Similarly, increasing BAT metabolic activity was associated inversely with PASP (P < 0.001), LVPWD (P = 0.01), relative wall thickness (P < 0.001) (Fig. 3d), mitral valve E/e' ratio (P = 0.002) and positively with mitral valve E/A ratio (P < 0.001) (Extended Data Fig. 5e). Other echocardiographic parameters did not exhibit associations with semi-quantitative BAT activity (Extended Data Fig. 5e). These data demonstrate that BAT presence and activity associate with decreased markers of left ventricular remodelling.

With regard to other medical conditions, patients with BAT had lower transaminase levels (P < 0.001) (Fig. 3e), lower alkaline phosphatase and higher albumin, and a lower percentage of patients had increased FIB-4 scores—a surrogate for the risk of advanced liver fibrosis[26] (Extended Data Fig. 5f). Parameters of systemic inflammation were also lower in patients with BAT, including total neutrophils (P < 0.001), neutrophil-to-lymphocyte ratio (P < 0.001) (Fig. 3e), platelets and erythrocyte sedimentation rate (Extended Data Fig. 5g). There was also a trend towards lower C-reactive protein in patients with BAT, with no changes in total white blood cells or lymphocytes (Extended Data Fig. 5g). We did not observe changes in renal or thyroid function in patients in the BAT$^+$ versus BAT$^-$ groups (Extended Data Fig. 5h). As patients with BAT showed a trend towards higher osteoporosis prevalence, available bone density scans were analysed. Patients with BAT had lower vertebral T-scores compared with patients in the BAT$^-$ group (P = 0.0026), with no changes in femoral neck T-scores (Fig. 3f).

Pharmacological regulators of BAT

To unravel pharmacologic determinants of BAT presence, we extracted home medication data 1 month before the index scan in patients from

our PSM cohort (Extended Data Fig. 6a). In total, 125 individual medications were assessed for associations with BAT status after exclusions (Extended Data Fig. 6a). Multi-variable logistic regression analyses identified that 39 of 125 medications exhibited a significant association with BAT status (Supplementary Table 6). Given that antibiotics are generally used in short courses, we excluded them from our list of chronic medications (Extended Data Fig. 6b). However, as modulation of the microbiome by antimicrobials could affect thermogenic fat[27], we performed a focused analysis on antibiotics and found that trimethoprim-sulfamethoxazole and several cephalosporins had positive associations with BAT status (Extended Data Fig. 6b).

Among our 39 candidate medications, we identified agents with known inhibitory effects on human BAT, such as β-blockers[9,28]. Specifically, atenolol (OR 0.42; 95% CI 0.27–0.64; $P < 0.001$) and propranolol (OR 0.38; 95% CI 0.20–0.74; $P = 0.02$) (Fig. 4a and Extended Data Fig. 6c) exhibited negative associations with BAT presence. Other known negative regulators of BAT, namely, selective serotonin re-uptake inhibitors (SSRIs)[29] such as fluoxetine (OR 0.33; 95% CI 0.21–0.51; $P < 0.001$), escitalopram (OR 0.60; 95% CI 0.48–0.75; $P < 0.001$) and sertraline (OR 0.57; 95% CI 0.44–0.75; $P < 0.001$) (Fig. 4a), were also associated negatively with BAT. Given that people with BAT had a lower prevalence of psychiatric disease, we performed analyses on psychiatric medications controlling for relevant psychiatric diagnoses (Supplementary Table 7), and demonstrated that SSRIs retain their negative association with BAT (Extended Data Fig. 6d). Among medications shown previously to activate BAT, we found that dexamethasone[30] was associated positively with BAT presence (OR 1.22; 95% CI 1.10–1.36; $P = 0.001$; Fig. 4a). Mirabegron—a β3-adrenergic agonist that promotes BAT activity in humans[13,31,32]—also showed a trend towards being associated with BAT positivity (Extended Data Fig. 6e). β2-adrenergic agonists (for example, inhaled salbutamol), which could promote BAT activity in humans[33,34], did not show a significant association (Supplementary Table 6). These findings demonstrate that our platform can identify most known modulators of human BAT and could uncover new pharmacological regulators of this tissue.

Among medications associated positively with BAT, we found hormonal modifiers (letrozole, leuprolide), antihypertensives (hydrochlorothiazide, amlodipine, losartan) and oral cancer drugs (osimertinib, lenalidomide). Based on expression of the target receptor and/or pathway in adipocytes[35], we focused on angiotensin receptor blockers (ARBs) as potential BAT-promoting drugs. The ARBs losartan (OR 1.36; 95% CI 1.13–1.63; $P = 0.006$) and valsartan (OR 1.52; 95% CI 1.14–2.02; $P = 0.02$) had significant positive associations with BAT^+ status, whereas irbesartan exhibited a non-statistically significant trend in the same direction (Fig. 4b).

Losartan enhances BAT activity through PPARγ

As proof of concept, we tested whether losartan increased the activity of differentiated brown adipocytes in vitro. First, we assessed whether losartan regulated uncoupling protein 1 (UCP1)—the main mediator of BAT thermogenesis. Losartan at low doses (10 μM) had no effect, whereas higher doses (50 μM and 100 μM) significantly increased *Ucp1* RNA levels in immortalized mature brown adipocytes (Extended Data Fig. 7a). Treatment with losartan at 50 μM induced an increase in *Ucp1* comparable with noradrenaline (NE)—a β-adrenergic agonist and known thermogenic activator (Fig. 4c); moreover, co-treatment with losartan and NE produced a synergistic effect on *Ucp1* (Fig. 4c). Losartan also increased RNA levels of other thermogenic genes such as *Pgc1a* (also known as *Ppargc1a*), *Elovl3* and *Cidea* (Extended Data Fig. 7b). A similar effect was seen in subcutaneous adipocytes enriched for beige adipocyte progenitors and, to a lesser extent, subcutaneous white adipocytes (Extended Data Fig. 7c). Losartan increased UCP1 protein in primary mature brown adipocytes at baseline and upon NE stimulation (Fig. 4d and Extended Data Fig. 7d). Finally, we assessed oxygen consumption rate in primary mature brown adipocytes and demonstrated that 72 h pretreatment with losartan significantly increased NE-dependent uncoupled respiration—a proxy for thermogenesis (Fig. 4e).

Similar to reports in human adipocytes[36], angiotensin II decreased *Ucp1* expression in mature brown adipocytes, whereas co-treatment with losartan rescued and further increased *Ucp1* expression, suggesting a possible angiotensin receptor 1 (AT1R)-independent mechanism (Extended Data Fig. 7e). We treated mature brown adipocytes with EXP3174, the active losartan metabolite (10–40% higher affinity for ATR1 than the parent compound) and EXP3179—a losartan metabolite with no affinity for ATR1 (refs. 37,38). Unexpectedly, EXP3179, but not EXP3174, increased *Ucp1* expression at baseline and in response to NE (Extended Data Fig. 7f,g). To further confirm that losartan acts independently of AT1R signalling, we knocked down *At1r* (Extended Data Fig. 7h) and showed that losartan still increased *Ucp1* expression. Knockdown of the receptor alone also seemed to affect *Ucp1* expression (Extended Data Fig. 7i), consistent with both AT1R-dependent and independent mechanisms.

Previous studies have suggested that some ARBs could act as direct PPARγ agonists[39]. We found that losartan and the inactive metabolite EXP3179, but not the active metabolite EXP3174, increased RNA levels of the classic PPARγ target *aP2* with and without NE stimulation (Extended Data Fig. 7j–l). Losartan also decreased RNA levels of PPARγ with no changes to adiponectin (Extended Data Fig. 7m) Thus, using a luciferase reporter system in HEK293T cells, we tested whether losartan and its inactive metabolite EXP3179 activate PPARγ directly. Increasing concentrations of losartan or EXP3179, but not EXP3174, resulted in augmented reporter activity (Fig. 4f). To test directly whether PPARγ mediates the increased *Ucp1* observed with losartan and EXP3179 in brown adipocytes, we co-treated cells with these compounds and a pharmacological inhibitor of PPARγ, GW9662, which binds the ligand-binding domain and prevents agonist-induced activation. Indeed, blocking PPARγ significantly attenuated the effects of losartan and its inactive metabolite on *Ucp1* RNA induction at baseline and upon NE stimulation (Fig. 4g and Extended Data Fig. 7n,o). Altogether, these data demonstrate that losartan increases UCP1 expression in brown adipocytes independently of AT1R signalling and by stimulating PPARγ transcriptional activity.

Finally, we investigated the effects of losartan on BAT physiology in vivo. Treating wild-type mice for 2 weeks with losartan at room temperature resulted in increased expression of *Ucp1* and other thermogenic genes in BAT with no significant changes to adipogenesis genes (Extended Data Fig. 8a,b). This was also observed at the protein level (Extended Data Fig. 8c,d). To functionally assess BAT thermogenic capacity, we acclimated losartan-treated mice and controls to thermoneutrality and then treated them acutely with the β3-agonist CL-316,243 (Extended Data Fig. 8e). BAT thermogenesis in response to β3 agonism (assessed by thermal camera) was higher in mice also receiving losartan compared with controls (Fig. 4h,i and Extended Data Fig. 8f).

To further assess the effects of losartan on whole-body energy expenditure, indirect calorimetry was performed in wild-type mice pre-treated with losartan in their drinking water for 10 days at room temperature (Extended Data Fig. 9a). Losartan-treated mice exhibited increased energy expenditure, O_2 consumption and CO_2 production, with no changes to their respiratory exchange ratio (RER), physical activity, food intake, body weight, fat mass or lean mass (Extended Data Fig. 9a–l). To examine the effects of losartan on cold stress, we pre-treated a separate cohort of wild-type mice at room temperature as above and performed indirect calorimetry at 4 °C (Extended Data Fig. 10a). Upon cold-induced BAT activation, losartan-treated mice again exhibited increased energy expenditure, O_2 consumption and CO_2 production, with no changes in RER (Fig. 4j,k and Extended Data Fig. 10b–e). This was independent of body weight, as assayed by analysis of covariance (Fig. 4l). There were no differences in locomotor activity and a trend towards increased food intake in losartan-treated mice (Extended Data Fig. 10f–h), which probably

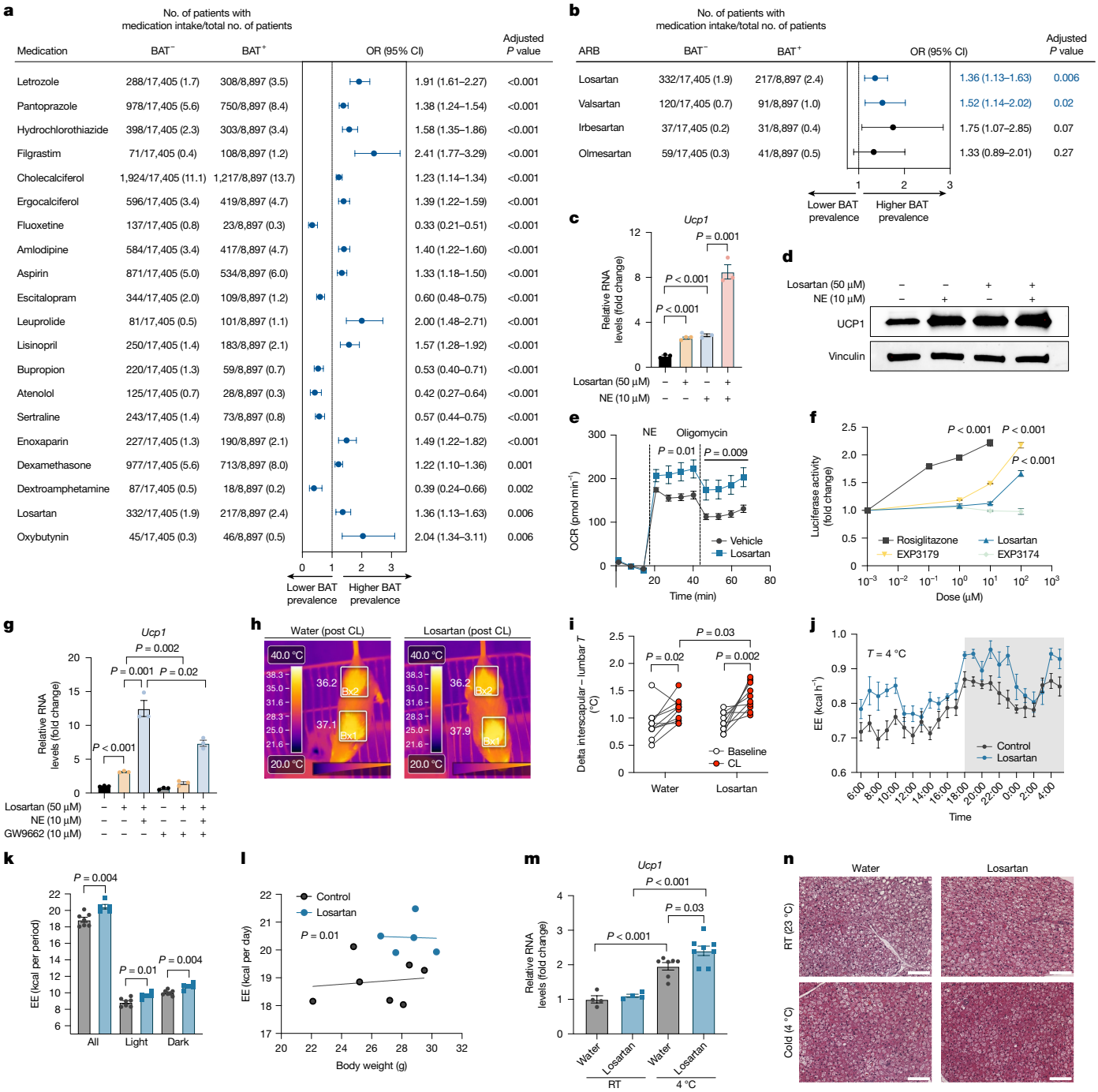


Fig. 4 | Associations of BAT with medications and effects of losartan. **a**,**b**, Forest plots showing ORs (circles) and 95% CIs (error bars) for associations of medications (**a**) and ARBs (**b**) with BAT status in the PSM cohort; *P* values, multi-variable logistic regression (Methods). **c**, *Ucp1* RNA levels in brown adipocytes pre-treated with losartan or vehicle ± NE. **d**, UCP1 immunoblot in brown adipocytes pre-treated with losartan or vehicle ± NE. **e**, Oxygen consumption rate in brown adipocytes pre-treated with losartan or vehicle ($n = 12$ technical replicates per group; squares, mean; error bars, s.e.m.). NE peak respiration and mean oxygen consumption rate during oligomycin were compared. **f**, PPARγ transcriptional activity in HEK293T cells treated with the compounds indicated ($n = 3$ biological replicates per treatment per dose; squares, mean; error bars, s.e.m. Experiment repeated twice); *P* values, one-way analysis of variance. **g**, *Ucp1* RNA levels in brown adipocytes pre-treated with GW9662 or vehicle and stimulated with losartan ± NE. **h**, Representative thermal camera images following CL-316243 injection in losartan-treated and control mice. **i**, BAT thermogenesis ($n = 10$ mice per group; white, baseline temperature; red, temperature after CL-316243 injection). Baseline versus after CL-316243 injection values, paired *t*-tests; after CL-316243 injection between groups, unpaired *t*-test. **j**–**l**, Energy expenditure in losartan-treated mice ($n = 7$) and controls ($n = 5$) at 4 °C: representative 24-h energy expenditure (circles, mean; error bars, s.e.m.) (**j**), mean 24-h, dark- and light-phase energy expenditure (**k**) and analysis of covariance of energy expenditure versus body weight (**l**); *P* value, simple linear regression and comparing slopes. **m**, BAT *Ucp1* RNA at room temperature ($n = 4$ mice per group) or after 5 days at 4 °C (losartan, $n = 8$; control, $n = 7$). **n**, Representative BAT haematoxylin and eosin images at room temperature or 4 °C. In **c** and **g**, dots represent biological replicates from one representative experiment. Experiments in **c**–**e** and **g** were repeated three times with similar results. *P* values in **c**,**e**,**g**,**k** and **m**, unpaired, two-tailed *t*-test. CL, CL-316243; EE, energy expenditure; OCR, oxygen consumption rate; RT, room temperature. Scale bars, 10 μm.

explains why body weight did not change (Extended Data Fig. 10i). Moreover, exposing mice treated with losartan to cold resulted in significantly increased BAT *Ucp1* (Fig. 4m), as well as smaller lipid droplets in brown adipocytes (Fig. 4n). We observed similar histologic findings in inguinal fat; however, there was no statistically significant increase in *Ucp1* expression (Extended Data Fig. 10j,k). Taken together, these data indicate that losartan treatment results in enhanced BAT activation and increased whole-body energy expenditure.

Discussion

Despite substantial advances, the therapeutic potential for targeting BAT to manage metabolic disease remains preliminary[5,6]. This retrospective study explored associations between BAT and human health in the largest cohort reported so far. We validated the strong link between BAT and cardiovascular diseases, while uncovering a previously undescribed association with psychiatric diseases. Our new machine learning approach allowed us to quantify depot-specific BAT metabolic activity rapidly and establish that the degree of BAT activity is linked to cardiometabolic health and healthier fat distribution. Finally, medication usage analysis uncovered a positive association between ARB use and BAT presence. Proof-of-concept in vitro and in vivo experiments confirmed that losartan activates brown adipocytes and promotes whole-body energy expenditure, demonstrating that our systems approach can identify pharmacologic agents that could be repurposed to activate BAT.

Numerous studies in mice have shown that BAT activation protects against obesity and hyperglycaemia through increased energy expenditure, clearance of circulating substrates and secretion of beneficial hormones and metabolites[40–42]. In humans, cold exposure and β-adrenergic agonists increase BAT metabolic activity, which correlates with improved glucose homeostasis[13,14]. Our study confirms that, among all diagnoses, BAT is associated primarily with decreased prevalence of cardiovascular diseases, improved glycaemic, lipid and inflammatory profiles, and evidence of decreased pathological cardiac remodelling. Our large-scale, depot-specific analysis allowed us to identify axillary BAT as being linked most strongly with beneficial metabolic outcomes and healthier WAT distribution. These findings highlight the heterogeneity of thermogenic adipose tissues in humans and the importance of dissecting their cellular and molecular characteristics[20–22].

AI tools such as ours will allow other groups to analyse BAT semi-quantitatively in their cohorts and expand these findings to other populations worldwide. This approach continues to rely on BAT glucose uptake on 18F-FDG-PET–CT scans, which may or may not correlate with BAT temperature and thermogenic capacity[43,44], and could be influenced significantly by insulin resistance[45]. To this point, we found that insulin-sensitizing medications such as metformin[46] were associated negatively with BAT presence (adjusting for diabetes status), and medications like olanzapine[47], which promote insulin resistance, were linked positively to BAT. This indicates that the clinical findings in our study cannot be explained simply by altered insulin sensitivity.

Beyond metabolic diseases, BAT presence was associated with a lower prevalence of anxiety and depression. This could be explained by studies linking healthier metabolic profiles and decreased visceral adiposity to lower rates of psychiatric disease[48–50]. Small studies have linked cold exposure—a known activator of BAT—to improved mental health[51,52]. Furthermore, BAT prevalence decreased with SSRI use, confirming findings from a recent, prospective human study[29]. Future studies focused on how BAT affects mood and behaviour, and the role of anti-depressants in this crosstalk are warranted. BAT presence was associated with lower prevalence of liver disease and improved hepatic function, consistent with previous studies[53,54]. Conversely, patients in the BAT^+ group showed a trend towards higher prevalence of osteoporosis and decreased lumbar bone mineral density, contrasting with previous reports linking cold-activated BAT with higher bone mineral density[55]. Although mouse studies suggest an endocrine connection between brown fat and bone[56], we cannot rule out that the observed association is specific to our cancer-centre-based cohort. Future trials on human BAT therapeutics should include assessment of bone health.

Our study uses a reverse translational approach, starting with a large human dataset that informs proof-of-concept experiments, to bridge the gap between predominantly mouse-based discoveries and human brown fat biology. Through this platform, we identified several ARBs that are associated positively with BAT and demonstrate that the medication used most widely in this family, losartan, directly activates brown adipocytes through PPARγ, independently of AT1R signalling. In vivo treatment with losartan at baseline and during a cold challenge resulted in increased whole-body energy expenditure. By contrast, a previous report described a role for losartan in beiging of white fat through AT1R-dependent apelin secretion[57]. Compared with losartan, its inactive metabolite EXP3179 exhibits higher PPARγ agonism in vitro, and it probably mediates most of the effects of losartan on BAT in vivo. In humans, chronic treatment with losartan resulted in increased serum levels of EXP3179 with a peak 2 h after treatment, and increased expression of PPARγ gene targets in circulating monocytes[37]. Treatment with ARBs has been associated with reductions in newly diagnosed diabetes[58], which could be linked to its effects on brown fat.

Our study has several limitations. First, its retrospective design highlights the need for large prospective studies; however, we controlled for several clinical confounders and validated the association of losartan with BAT experimentally. Second, 18F-FDG-PET–CT scans were obtained without previous cold exposure, potentially underestimating BAT prevalence. Third, our convenience cohort was derived from a cancer centre and, despite controlling extensively for cancer-related variables, we cannot exclude effects from tumour types or cancer therapies. For instance, BAT is linked to higher breast cancer prevalence, lower odds of gastrointestinal malignancies and higher usage of cancer treatments such as mitotic inhibitors. Studies in mice have suggested activation of BAT reduces cancer progression by decreasing available circulating glucose for tumour metabolism[59]. To our knowledge, there is no literature demonstrating direct effects of mitotic inhibitors or other cancer therapies on brown adipocytes, and future studies of these associations are warranted. Until a reliable biomarker or non-invasive test for BAT is established, a large, prospective study involving 18F-FDG-PET–CT in the non-oncologic setting is highly implausible. At present, a large PSM cohort is the most feasible approach to assess BAT and clinical phenotypes comprehensively in humans.

In conclusion, we describe new associations between BAT and clinical outcomes through big data and AI-based analyses. Our systems-approach provides a resource for the field and can be extended to study other regulators of BAT such as genetics. Finally, our proof-of-concept studies demonstrate that losartan activates brown adipocytes through a PPARγ dependent mechanism, raising the possibility that this agent could be repurposed to activate BAT in humans.

Online content

Any methods, additional references, Nature Portfolio reporting summaries, source data, extended data, supplementary information, acknowledgements, peer review information; details of author contributions and competing interests; and statements of data and code availability are available at https://doi.org/10.1038/s41586-026-11162-7.

1. Rosen, E. D. & Spiegelman, B. M. What we talk about when we talk about fat. *Cell* **156**, 20–44 https://doi.org/10.1016/j.cell.2013.12.012 (2014).
2. Gonzalez-Muniesa, P. et al. Obesity. *Nat. Rev. Dis. Primers* **3**, 17034 https://doi.org/10.1038/nrdp.2017.34 (2017).
3. Cohen, P. & Kajimura, S. The cellular and functional complexity of thermogenic fat. *Nat. Rev. Mol. Cell Biol.* **22**, 393–409 https://doi.org/10.1038/s41580-021-00350-0 (2021).
4. Becher, T. et al. Brown adipose tissue is associated with cardiometabolic health. *Nat. Med.* **27**, 58–65 https://doi.org/10.1038/s41591-020-1126-7 (2021).

5. Cypess, A. M. et al. Emerging debates and resolutions in brown adipose tissue research. *Cell Metab.* **37**, 12–33 https://doi.org/10.1016/j.cmet.2024.11.002 (2025).
6. Gupta, R. K. Human brown fat and metabolic disease: a heated debate. *J. Clin. Invest.* **133**, e176678 https://doi.org/10.1172/JCI176678 (2023).
7. Valenzuela, P. L. et al. Obesity and the risk of cardiometabolic diseases. *Nat. Rev. Cardiol.* **20**, 475–494 https://doi.org/10.1038/s41569-023-00847-5 (2023).
8. Gesta, S., Tseng, Y. H. & Kahn, C. R. Developmental origin of fat: tracking obesity to its source. *Cell* **131**, 242–256 https://doi.org/10.1016/j.cell.2007.10.004 (2007).
9. Cypess, A. M. et al. Identification and importance of brown adipose tissue in adult humans. *N. Engl. J. Med.* **360**, 1509–1517 https://doi.org/10.1056/NEJMoa0810780 (2009).
10. van Marken Lichtenbelt, W. D. et al. Cold-activated brown adipose tissue in healthy men. *N. Engl. J. Med.* **360**, 1500–1508 https://doi.org/10.1056/NEJMoa0808718 (2009).
11. Virtanen, K. A. et al. Functional brown adipose tissue in healthy adults. *N. Engl. J. Med.* **360**, 1518–1525 https://doi.org/10.1056/NEJMoa0808949 (2009).
12. Saito, M. et al. High incidence of metabolically active brown adipose tissue in healthy adult humans: effects of cold exposure and adiposity. *Diabetes* **58**, 1526–1531 https://doi.org/10.2337/db09-0530 (2009).
13. O'Mara, A. E. et al. Chronic mirabegron treatment increases human brown fat, HDL cholesterol, and insulin sensitivity. *J. Clin. Invest.* **130**, 2209–2219 https://doi.org/10.1172/JCI131126 (2020).
14. Hanssen, M. J. et al. Short-term cold acclimation improves insulin sensitivity in patients with type 2 diabetes mellitus. *Nat. Med.* **21**, 863–865 https://doi.org/10.1038/nm.3891 (2015).
15. Chondronikola, M. et al. Brown adipose tissue improves whole-body glucose homeostasis and insulin sensitivity in humans. *Diabetes* **63**, 4089–4099 https://doi.org/10.2337/db14-0746 (2014).
16. Chondronikola, M. et al. Brown adipose tissue activation is linked to distinct systemic effects on lipid metabolism in humans. *Cell Metab* **23**, 1200–1206 https://doi.org/10.1016/j.cmet.2016.04.029 (2016).
17. Orava, J. et al. Different metabolic responses of human brown adipose tissue to activation by cold and insulin. *Cell Metab* **14**, 272–279 https://doi.org/10.1016/j.cmet.2011.06.012 (2011).
18. Leitner, B. P. et al. Mapping of human brown adipose tissue in lean and obese young men. *Proc. Natl Acad. Sci. USA* **114**, 8649–8654 https://doi.org/10.1073/pnas.1705287114 (2017).
19. Lafontaine, D. et al. Brown adipose tissue machine learning nnU-Net V2 network using TriDFusion (3DF). *EJNMMI Res.* **15**, 108 https://doi.org/10.1186/s13550-025-01303-w (2025).
20. Ziegler, A. K. & Scheele, C. Human adipose depots' diverse functions and dysregulations during cardiometabolic disease. *NPJ Metab. Health Dis.* **2**, 34 https://doi.org/10.1038/s44324-024-00036-z (2024).
21. Lidell, M. E. et al. Evidence for two types of brown adipose tissue in humans. *Nat. Med.* **19**, 631–634 https://doi.org/10.1038/nm.3017 (2013).
22. Sacks, H. & Symonds, M. E. Anatomical locations of human brown adipose tissue: functional relevance and implications in obesity and type 2 diabetes. *Diabetes* **62**, 1783–1790 https://doi.org/10.2337/db12-1430 (2013).
23. Jung, H. N. et al. Remnant cholesterol as an independent cardiovascular risk factor in young adults: an age-stratified cohort study. *J. Am. Coll. Cardiol.* **86**, 2047–2058 https://doi.org/10.1016/j.jacc.2025.09.015 (2025).
24. Raiko, J., Orava, J., Savisto, N. & Virtanen, K. A. High brown fat activity correlates with cardiovascular risk factor levels cross-sectionally and subclinical atherosclerosis at 5-year follow-up. *Arterioscler. Thromb. Vasc. Biol.* **40**, 1289–1295 https://doi.org/10.1161/ATVBAHA.119.313806 (2020).
25. Koenen, M. et al. Ablation of Prdm16 and beige fat identity causes vascular remodeling and elevated blood pressure. *Science* **391**, 306–313 https://doi.org/10.1126/science.ady8644 (2026).
26. Wattacheril, J. J., Abdelmalek, M. F., Lim, J. K. & Sanyal, A. J. AGA clinical practice update on the role of noninvasive biomarkers in the evaluation and management of nonalcoholic fatty liver disease: expert review. *Gastroenterology* **165**, 1080–1088 https://doi.org/10.1053/j.gastro.2023.06.013 (2023).
27. Li, B. et al. Microbiota depletion impairs thermogenesis of brown adipose tissue and browning of white adipose tissue. *Cell Rep.* **26**, 2720–2737 https://doi.org/10.1016/j.celrep.2019.02.015 (2019).
28. Potzsch, C. et al. Prevention of activated brown adipose tissue on (18)F-FDG-PET scans of young lymphoma patients: results of an ancillary study within the EuroNet-PHL-C2 trial. *Sci. Rep.* **13**, 21944 https://doi.org/10.1038/s41598-023-48871-2 (2023).
29. Suchacki, K. J. et al. The serotonin transporter sustains human brown adipose tissue thermogenesis. *Nat. Metab.* **5**, 1319–1336 https://doi.org/10.1038/s42255-023-00839-2 (2023).
30. Ramage, L. E. et al. Glucocorticoids acutely increase brown adipose tissue activity in humans, revealing species-specific differences in UCP-1 regulation. *Cell Metab* **24**, 130–141 https://doi.org/10.1016/j.cmet.2016.06.011 (2016).
31. Cypess, A. M. et al. Activation of human brown adipose tissue by a beta3-adrenergic receptor agonist. *Cell Metab.* **21**, 33–38 https://doi.org/10.1016/j.cmet.2014.12.009 (2015).
32. Finlin, B. S. et al. The beta3-adrenergic receptor agonist mirabegron improves glucose homeostasis in obese humans. *J. Clin. Invest.* **130**, 2319–2331 https://doi.org/10.1172/JCI134892 (2020).
33. Blondin, D. P. et al. Human brown adipocyte thermogenesis is driven by beta2-AR stimulation. *Cell Metab* **32**, 287–300 https://doi.org/10.1016/j.cmet.2020.07.005 (2020).
34. Straat, M. E. et al. Stimulation of the beta-2-adrenergic receptor with salbutamol activates human brown adipose tissue. *Cell Rep. Med.* **4**, 100942 https://doi.org/10.1016/j.xcrm.2023.100942 (2023).
35. Pahlavani, M., Kalupahana, N. S., Ramalingam, L. & Moustaid-Moussa, N. Regulation and functions of the renin-angiotensin system in white and brown adipose tissue. *Compr. Physiol.* **7**, 1137–1150 https://doi.org/10.1002/cphy.c160031 (2017).
36. Takeda, Y., Yoshikawa, T. & Dai, P. Angiotensin II participates in mitochondrial thermogenic functions via the activation of glycolysis in chemically induced human brown adipocytes. *Sci. Rep.* **14**, 10789 https://doi.org/10.1038/s41598-024-61774-0 (2024).
37. Kappert, K. et al. Chronic treatment with losartan results in sufficient serum levels of the metabolite EXP3179 for PPARgamma activation. *Hypertension* **54**, 738–743 https://doi.org/10.1161/HYPERTENSIONAHA.109.132886 (2009).
38. Sica, D. A., Gehr, T. W. & Ghosh, S. Clinical pharmacokinetics of losartan. *Clin. Pharmacokinet.* **44**, 797–814 https://doi.org/10.2165/00003088-200544080-00003 (2005).
39. Janke, J. et al. Angiotensin type 1 receptor antagonists induce human in-vitro adipogenesis through peroxisome proliferator-activated receptor-gamma activation. *J. Hypertens.* **24**, 1809–1816 https://doi.org/10.1097/01.hjh.0000242405.68461.84 (2006).
40. Wolfrum, C. & Gerhart-Hines, Z. Fueling the fire of adipose thermogenesis. *Science* **375**, 1229–1231 https://doi.org/10.1126/science.abl7108 (2022).
41. Cannon, B. & Nedergaard, J. Brown adipose tissue: function and physiological significance. *Physiol. Rev.* **84**, 277–359 https://doi.org/10.1152/physrev.00015.2003 (2004).
42. Choi, C. H. J. et al. LRG1 is an adipokine that promotes insulin sensitivity and suppresses inflammation. *eLife* **11**, e81559 https://doi.org/10.7554/eLife.81559 (2022).
43. Koskensalo, K. et al. Human brown adipose tissue temperature and fat fraction are related to its metabolic activity. *J. Clin. Endocrinol. Metab.* **102**, 1200–1207 https://doi.org/10.1210/jc.2016-3086 (2017).
44. Blondin, D. P. et al. Selective impairment of glucose but not fatty acid or oxidative metabolism in brown adipose tissue of subjects with type 2 diabetes. *Diabetes* **64**, 2388–2397 https://doi.org/10.2337/db14-1651 (2015).
45. Orava, J. et al. Blunted metabolic responses to cold and insulin stimulation in brown adipose tissue of obese humans. *Obesity* **21**, 2279–2287 https://doi.org/10.1002/oby.20456 (2013).
46. Zhou, G. et al. Role of AMP-activated protein kinase in mechanism of metformin action. *J. Clin. Invest.* **108**, 1167–1174 https://doi.org/10.1172/JCI13505 (2001).
47. Drici, M. D. & Priori, S. Cardiovascular risks of atypical antipsychotic drug treatment. *Pharmacoepidemiol. Drug Saf.* **16**, 882–890 https://doi.org/10.1002/pds.1424 (2007).
48. Luppino, F. S. et al. Overweight, obesity, and depression: a systematic review and meta-analysis of longitudinal studies. *Arch. Gen. Psychiatry* **67**, 220–229 https://doi.org/10.1001/archgenpsychiatry.2010.2 (2010).
49. Yang, W. et al. The increased prevalence of depression and anxiety in T2DM patients associated with blood glucose fluctuation and sleep quality. *BMC Endocr. Disord.* **22**, 232 https://doi.org/10.1186/s12902-022-01147-8 (2022).
50. Chourpiliadis, C. et al. Metabolic profile and long-term risk of depression, anxiety, and stress-related disorders. *JAMA Netw. Open* **7**, e244525 https://doi.org/10.1001/jamanetworkopen.2024.4525 (2024).
51. van Tulleken, C., Tipton, M., Massey, H. & Harper, C. M. Open water swimming as a treatment for major depressive disorder. *BMJ Case Rep.* https://doi.org/10.1136/bcr-2018-225007 (2018).
52. Yankouskaya, A., Williamson, R., Stacey, C., Totman, J. J. & Massey, H. Short-term head-out whole-body cold-water immersion facilitates positive affect and increases interaction between large-scale brain networks. *Biology* **12**, 211 https://doi.org/10.3390/biology12020211 (2023).
53. Shen, H., Jiang, L., Lin, J. D., Omary, M. B. & Rui, L. Brown fat activation mitigates alcohol-induced liver steatosis and injury in mice. *J. Clin. Invest.* **129**, 2305–2317 https://doi.org/10.1172/JCI124376 (2019).
54. Herz, C. T. et al. Active brown adipose tissue is associated with a healthier metabolic phenotype in obesity. *Diabetes* https://doi.org/10.2337/db21-0475 (2021).
55. Lee, P. et al. Cold-activated brown adipose tissue is an independent predictor of higher bone mineral density in women. *Osteoporos. Int.* **24**, 1513–1518 https://doi.org/10.1007/s00198-012-2110-y (2013).
56. Wang, T. et al. Whitening of brown adipose tissue inhibits osteogenic differentiation via secretion of S100A8/A9. *iScience* **27**, 108857 https://doi.org/10.1016/j.isci.2024.108857 (2024).
57. Kim, D. Y. et al. Angiotensin AT(1) receptor antagonism by losartan stimulates adipocyte browning via induction of apelin. *J. Biol. Chem.* **295**, 14878–14892 https://doi.org/10.1074/jbc.RA120.013834 (2020).
58. Abuissa, H., Jones, P. G., Marso, S. P. & O'Keefe, J. H. Jr. Angiotensin-converting enzyme inhibitors or angiotensin receptor blockers for prevention of type 2 diabetes: a meta-analysis of randomized clinical trials. *J. Am. Coll. Cardiol.* **46**, 821–826 https://doi.org/10.1016/j.jacc.2005.05.051 (2005).
59. Seki, T. et al. Brown-fat-mediated tumour suppression by cold-altered global metabolism. *Nature* **608**, 421–428 https://doi.org/10.1038/s41586-022-05030-3 (2022).

Publisher's note Springer Nature remains neutral with regard to jurisdictional claims in published maps and institutional affiliations.

Open Access This article is licensed under a Creative Commons Attribution-NonCommercial-NoDerivatives 4.0 International License, which permits any non-commercial use, sharing, distribution and reproduction in any medium or format, as long as you give appropriate credit to the original author(s) and the source, provide a link to the Creative Commons licence, and indicate if you modified the licensed material. You do not have permission under this licence to share adapted material derived from this article or parts of it. The images or other third party material in this article are included in the article's Creative Commons licence, unless indicated otherwise in a credit line to the material. If material is not included in the article's Creative Commons licence and your intended use is not permitted by statutory regulation or exceeds the permitted use, you will need to obtain permission directly from the copyright holder. To view a copy of this licence, visit http://creativecommons.org/licenses/by-nc-nd/4.0/.

© The Author(s) 2026

Methods

Study design and participants

This retrospective case–control study followed institutional guidelines and was approved by the Institutional Review Board of Memorial Sloan Kettering Cancer Center (MSK), protocol number 17-581. The requirement for informed consent was waived because the study involved secondary analysis of previously acquired PET–CT imaging and clinical data, posed no more than minimal risk to participants and could not be conducted practically with individual informed consent. All patient data were deidentified before use.

We previously established a cohort of patients with BAT by analysing 18F-FDG-PET–CT scans performed at MSK from June 2009 through March 2018[4]. Patients who were positive for BAT in at least one scan were termed BAT^+, whereas the remaining patients were grouped as BAT^-. To expand this cohort, we established a new Extension BAT Cohort by following a similar strategy. We reviewed all 18F-FDG-PET–CT scans performed at MSK from patients aged 18 years and above from April 2018 through July 2024. People who were positive for BAT on at least one scan were termed BAT^+, whereas the remaining patients were grouped as BAT^- (Extended Data Fig. 1a and Supplementary Fig. 2). For each patient in both groups, an index scan was designated: in patients with BAT reported on at least one 18F-FDG-PET–CT scan, the first scan that reported BAT was defined as the index scan. In patients without BAT on any scan, the first 18F-FDG-PET–CT scan served as the index scan. We collected demographic, BMI, outside temperature data and pertinent ICD-9 and ICD-10 codes corresponding to cardiometabolic diseases[4] (1 year after the index scan) (Supplementary Table 8) from the institutional EHR. Average outdoor temperatures in New York City were obtained from the US National Weather Service. An initial logistic regression analysis was performed on patients in the BAT^+ versus BAT^- groups who belonged exclusively to the Extension BAT Cohort to establish associations between BAT presence and cardiometabolic diseases. As the association of BAT presence with reduced prevalence of cardiometabolic disease was confirmed in the Extension BAT Cohort (Extended Data Fig. 1b), we proceeded to merge the Established BAT Cohort with the Extension BAT Cohort to create an Expanded BAT Cohort (Extended Data Fig. 1a). If a patient was present in both cohorts, data from the Established BAT Cohort were used.

Data collection and PSM

To create a balanced study cohort derived from the Expanded BAT Cohort, patients in the BAT^+ and BAT^- groups were matched using PSM. Propensity scores were estimated using a non-parsimonious multi-variable logistic regression model with BAT status (presence or absence) as the dependent variable and age, sex, BMI and temperature at time of scan as co-variates. Matching was performed using a greedy nearest neighbour matching algorithm without replacement, with a calliper width set to 0.2 and a matching ratio of 1:2. This resulted in a final study cohort of 26,302 (8,897 BAT^+ and 17,405 BAT^-). Balance diagnostics were performed to assess the success of the matching procedure using standardized mean differences for all variables included in the propensity score model before and after matching. Postmatching standardized mean differences within the range of −0.10 to 0.10 indicated adequate balance between the BAT^+ and BAT^- groups across all measured co-variates, supporting the validity of the PSM design for causal inference.

We collected pertinent clinical data for each patient as described previously[4]. In brief, for cancer site, we included the specific cancer diagnostic code (ICD-0) listed closest to the index scan date (Supplementary Table 1). Data referring to cancer treatment were collected if administered within 90 days before the index scan and classified as previously[4] (Supplementary Table 2). Pertinent ICD-9 and ICD-10 codes corresponding to cardiometabolic diseases[4] (Supplementary Table 8) and all other codes were extracted up to 1 year after the index scan in patients from our PSM cohort. Codes were selected to represent non-paediatric, non-obstetric, adult disorders as explained below.

For laboratory values, clinical indices and imaging studies, we extracted available data up to 1 year after the index scan in our PSM cohort. Analyses were performed in BAT^+ and BAT^- patients with available values. To identify individual pharmacological agents associated with BAT presence, we extracted medications in the home medication list and/or medications with an active pharmacy prescription in the EHR from each patient belonging to our PSM cohort. We included only medications listed up to 1 month before the index scan for each patient. We excluded pharmacological agents with unlikely systemic effects, such as those with topical, ophthalmic, nasal and otic administration. Antimicrobials were excluded as they are generally prescribed in short courses. Medications classified as 'as needed' and herbal supplements were excluded. Medications with low frequency counts (present in fewer than 40 patients) were excluded. A final list of medications included in the analyses can be found in Supplementary Table 9. These medications were also grouped by general categories as described in Supplementary Table 9.

Selection of diagnostic codes for unbiased associations with BAT

To explore unbiased associations between BAT and other diseases, we extracted from the EHR diagnostic codes (ICD-9 and ICD-10) listed up to 1 year after the index scan from patients belonging to our PSM cohort. To select the codes for extraction, we grouped ICD-9 and ICD-10 codes based on their first three letters and/or digits. ICD-10 codes belonging to general groupings: A, B, C, D, E, F, G, H, I, J, K, L, M, N and R were included as they group the medical pathologies most likely to be found in a non-paediatric, non-obstetric, adult cancer population. A similar rationale was used for the selection of ICD-9 codes. A total of 1,157 ICD-10 codes and 626 ICD-9 codes were queried for extraction from the EHR.

After code extraction, to avoid redundancy we merged ICD-9 codes with their corresponding ICD-10 codes based on a manual review of each code. The nomenclature of the ICD-10 code was maintained for downstream analysis in cases where an ICD-10 and ICD-9 code were merged. ICD-9 codes that did not have a corresponding ICD-10 code were maintained with their nomenclature. This left us with a total of 1,209 codes between individual ICD-9 and merged ICD-9 and ICD-10 codes.

To further filter diagnostic codes for analyses, we excluded codes with low frequencies (present in fewer than 40 patients) and those referring to a cancer diagnosis (Supplementary Table 1) given all patients had a cancer site assigned already. This left us with a final list of 511 diagnostic codes. Given the large number of codes, we initially performed a screening analysis using a univariable logistic regression analysis to identify unadjusted associations of the 511 with the presence of BAT. A total of 104 codes were associated significantly with BAT status in this analysis. Subsequently, we analysed each of these 104 codes using a multi-variable regression analysis to assess their individual association with BAT, while controlling for age, sex, BMI, ambient temperature, self-reported race and ethnicity, smoking history, family history of cardiovascular disease, cancer site, cancer stage, cancer treatment and general groups of outpatient medications (Extended Data Fig. 1a).

Machine learning approach to quantify BAT activity

The 3DF workflow[19] used PET and CT images in DICOM format. Using information from the DICOM header regarding image orientation and patient spatial positioning, the PET image was resampled to match the dimensions of the CT image through linear interpolation. Both PET and CT images were then converted into the .nrrd file format and processed by nnU-net. The nnU-net model produced a mask prediction where each pixel value corresponds to an anatomical site: 1 for cervical, 2 for supraclavicular, 3 for mediastinal, 4 for paraspinal, 5 for axillary and

6 for abdominal regions. The mask predictions were interpreted by 3DF, and contours were generated. These contours were down-sampled to match the original PET image dimensions, and metrics from the original PET for each anatomical site were exported to an Excel master file. The 3DF process was executed in batch mode, with several instances running simultaneously to efficiently segment a large cohort. We used this method to quantify BAT metabolic activity in 8,709 patients in the BAT^+ group from our cohort. A small portion of patients (n = 188) in the BAT^+ group could not be quantified due to differences in field of view between the CT and PET image.

Machine learning approach to quantify SAT and VAT area

The 3DF[19,60] abdominal adipose tissue workflow was performed on axial CT images at the L3–L4 intervertebral disc level. The target slice was identified automatically using TotalSegmentator[61] vertebral segmentation, with the analysis slice defined as the midpoint between the inferior extent of the L3 mask and the superior extent of the L4 mask. The outer body contour on the selected slice was derived by thresholding voxels above −500 Hounsfield units, followed by hole filling, removal of small components, retention of the largest connected component and morphological closing. Outer abdominal circumference was then calculated from the resulting body boundary using DICOM pixel spacing. Adipose tissue was quantified using a hybrid attenuation and AI-based method. Fat voxels were first identified within the body contour using an attenuation range of −195 to −45 Hounsfield units, and these voxels were then partitioned into SAT and VAT using TotalSegmentator tissue-type compartment masks. The outer abdominal circumference (in centimetres), SAT area (in square centimetres), VAT area (in square centimetres) and subcutaneous-to-visceral ratio were exported to an Excel master file. We used this method to quantify WAT distribution parameters in 8,040 patients with BAT from our cohort.

Selection of medications for testing in animal and mouse models

Multi-variable logistic regression analysis revealed that 39 out of 125 individual medications exhibited a significant association with BAT, as depicted in Supplementary Table 6. Of 38 medications examined, 29 had a positive association with the presence of BAT, suggesting that they could act as activators of this tissue. To select candidates for testing, we performed a literature search for each medication focusing on the following criteria: (1) expression of the target receptor and/or pathway in adipocytes, (2) direct effects of the medication in adipocytes and (3) potential cardiometabolic benefits beyond their intended pharmacologic effect. Out of 29 medications, losartan and valsartan fulfilled these criteria.

Cellular studies in adipocytes

Immortalized and primary brown adipocytes were cultured and differentiated as described previously[42], and experiments were performed on mature brown adipocytes on days 7–10 of differentiation. Immortalized cell line tested negative for mycoplasma. Mature brown adipocytes were treated with losartan potassium (Sigma, catalogue no. SML3269) for 24–72 h before experiments. Several doses of losartan (10 μM, 50 μM and 100 μM) were tested initially, and subsequent experiments were done with losartan at a 50-μM dose. NE at a concentration of 10 μM was used to stimulate Ucp1 transcription and activity. For experiments testing losartan metabolites, EXP3174 from Selleckchem (catalogue no. S5980) was used at a dose of 50 μM, and EXP3179 from Cayman (catalogue no. 18855) was used at a dose of 50 μM. For PPARγ inhibition in mature brown adipocytes, GW9662 from Sigma (catalogue no. M6191) was used at a dose of 10 μM. Cells were then collected and processed for downstream RNA and protein analyses. Respirometry on mature adipocytes was performed in 96-well plates per the manufacturer's instructions (Seahorse, Agilent).

As a model for beige and white adipocytes, we isolated the stromal vascular fraction from the inguinal region (enriched in beige adipocyte progenitor cells) and the dorsolumbar region (enriched in white adipocyte progenitor cells) from the inguinal fat depot of 4-week-old mice. Stromal vascular fraction cells from these two regions were plated and differentiated as described previously by our group[62,63]. Enrichment for adipocytes derived from beige progenitors was confirmed by *Ucp1* expression. Cells were then treated with losartan ± NE as described above for brown adipocytes.

shRNA-mediated knockdown in brown adipocytes

shRNA sequences targeting *At1r* were obtained from the Broad Institute's Genetic Perturbation Platform. Oligonucleotides 58 bp in length containing the targeting sequence GCCAGTGTCTTTCTTCTAAAT were cloned in the pLKO.1 vector from Addgene. The pLKO.1-TRC cloning vector was a gift from D. Root (Addgene plasmid, catalogue no. 10878)[64]. The pLKO.1-shRNAs, pMD2.G and psPAX three-package system were used to construct a silencing-expression lentivirus in HEK293T cells. Cells tested negative for mycoplasma. Primary brown adipocytes were transduced with lentivirus on day 2 of differentiation, and puromycin selection was started at day 4. Cells were used for experiments with losartan once fully differentiated (day 6 and onwards).

PPARγ luciferase reporter assay

HEK293T cells were transfected using Fugene HD (Promega) with plasmids containing PPARγ2 (pBabe bleo human PPARγ2), RXRa (pSV Sport RXRa), PPRE (DR1X3) firefly luciferase reporter (PPRE X3-TK-luc) and renilla luciferase (pRL-TK-Renilla, Promega). PPRE X3-TK-luc (Addgene plasmid, catalogue no. 1015) and pSV Sport RXRa (Addgene plasmid, catalogue no. 8882) were a kind gift from B. Spiegelman[65,66]. pBabe bleo human PPARγ2 (Addgene plasmid, catalogue no. 11439) was a kind gift from C. R. Kahn. Following an overnight transfection, cells were treated with cells with increasing concentrations of losartan, EXP3179, EXP3174 and rosiglitazone as a positive control. Cells were lysed and processed for luciferase assays according to the Dual-Luciferase Reporter Assay System (Promega) protocol.

Animal studies and metabolic phenotyping

All animals in this study were male mice on a C57BL/6J background and maintained on a 12-h light–dark cycle with free access to food and water. All mice were housed at 23 °C and fed with a standard rodent chow diet. Animal care and experimentation were performed according to procedures approved by the Institutional Animal Care and Use Committees at the Rockefeller University (24019-H) and Weill Cornell Medicine (2017-0043).

For animal studies using losartan, 10- to 14-week-old C57BL/6J wild-type mice were treated with 100 mg kg^{-1} d^{-1} losartan by oral gavage twice a day, or losartan dissolved in their drinking water at the same dose. Water intake per mouse was monitored every 48 h to 72 h to warrant the above dose was maintained throughout the experiments. Mice were randomized to treatment, and investigators were not blinded. Sample size was determined based on preliminary experiments. Mice were then euthanized and BAT was collected for protein and RNA analyses.

For assessment of BAT-specific heat production, we used forward-looking infrared (FLIR) thermography using a Teledyne FLIR E96 infrared camera with emissivity set to 0.98. C57BL/6J wild-type mice were treated with 100 mg kg^{-1} d^{-1} losartan dissolved in their drinking water for 1 week at room temperature, after which mice were acclimated to thermoneutrality (28 °C) for 1 week before image acquisition. Mice were anaesthetized under isoflurane gas 4 days before experiments, at which point we shaved a 2 × 2-cm region in the midline interscapular and midline lumbar regions. We briefly applied Nair hair removal cream to the shaved regions to ensure lasting skin exposure. Mice were monitored during and after anaesthesia and shaving to ensure full recovery and minimal irritation. After 1 week at thermoneutrality, mice were injected with 1 mg kg^{-1} of CL-316243 and 2 h later thermal images were

captured by gently suspending non-anaesthetized mice by the tail. Duplicate images for each mouse were analysed using FLIR Thermal Studio software. We considered the average maximum temperature recorded in each shaved region as indicators of interscapular and lumbar temperature. The absolute temperature difference between interscapular and lumbar temperature was used to quantify BAT thermogenesis, as reported previously by other researchers[67–70].

Whole-body metabolic measurements were performed using a Promethion Metabolic Screening System for Mice (Sable Systems International). Mice were housed individually with ad libitum access to standard chow diet and given either drinking or losartan water under a 12-h light–dark cycle. Before experimentation, mice were housed singly and acclimatized to room temperature (22 °C) for 10 days within temperature-controlled environmental enclosures (DB034 Laboratory Incubator, Darwin Chambers). For the cold exposure challenge, mice were transferred to a 4 °C environmental chamber and maintained in metabolic cages with a consistent volume of pine chip bedding, without cotton nesting squares for a 5-day experiment. Losartan was administered in drinking water at the indicated concentration throughout the study period, and water intake was monitored continuously. Rates of oxygen consumption and carbon dioxide production were acquired by indirect calorimetry with a sampling frequency of 1 s. Respirometry values were determined every 5 min; the dwell time for each cage was 30 s, with baseline cage sampling frequency of 30 s occurring every four cages[71]. Data were processed further as hourly values and cumulative measurements over 24-h periods, including separate analyses for light and dark phases.

Energy expenditure was assessed using indirect calorimetry and calculated using the Weir equation[72]. Distance travelled (activity) is determined by *x* and *y* position displacements represented by beam breaks within a grid of infrared sensors built into each cage (PedMeters and AllMeters). Food and water intake were recorded automatically. Body weight was measured before, before 4°C exposure and at the end of the study. Animals were monitored daily to ensure health and stability during cold exposure. Raw data were subjected to chamber-level quality control before to analysis. Fat and lean mass were determined using EchoMRI analysis.

Data acquisition and instrument control were coordinated by IM-3 software, and the resulting raw data were processed with Macro Interpreter v.2.38 (Sable Systems) using an analysis script detailing all aspects of data transformation (One-click macro v.2.45; Sable Systems). Indirect calorimetric data were analysed using Excel, R and validated using CalR and graphed using GraphPad Prism v.11.

RNA isolation, cDNA synthesis and real-time PCR

For RNA extraction from cultured mature adipocytes, cells were lysed in RLT buffer (Qiagen) and RNA was extracted using RNeasy Micro and Mini kits (Qiagen). cDNA was synthesized through reverse transcription using a cDNA synthesis kit (Applied Biosciences). cDNA was analysed by real-time PCR using specific gene primers and a SYBR Green Master Mix (Life Technologies). Relative fold changes of mRNA levels were calculated using the ΔCT method with cyclophilin as loading control. A list of primer sequences can be found in Supplementary Table 10.

Protein extraction and western blot

For protein extraction from cultured adipocytes and tissue from mice, cells and/or tissue were lysed in radioimmunoprecipitation assay buffer with protease inhibitor cocktail and phosphatase inhibitor cocktail. Protein extracts were resolved on pre-cast polyacrylamide gels (BioRad, 4–20% Mini PROTEAN) and transferred to a polyvinylidene fluoride membrane. Membranes were incubated overnight at 4 °C with appropriate primary antibodies. Detection of proteins was carried out by incubation with horseradish peroxidase-conjugated secondary antibodies followed by enhanced chemiluminescence detection reagents. Band density was quantified using Fiji/ImageJ (National Institutes of Health (NIH)).

Statistical analysis

The association between BAT and age, BMI and temperature was assessed by a Pearson's correlation coefficient. Prevalence of BAT in men and women was compared using a chi-squared test.

To assess whether BAT status was a predictor of cardiometabolic diseases in the PSM cohort, we used multi-variable logistic regression adjusting for age, sex, BMI, ambient temperature, self-reported race and ethnicity, smoking history, family history of cardiovascular disease, cancer site, cancer stage, cancer treatment and general groups of outpatient medications. BAT metabolic activity (total and depot-specific) was calculated as the product of SUV mean and BAT volume (in millilitres) and stratified into tertiles. The association of BAT activity with cardiometabolic diseases was assessed using a multi-variable logistic regression adjusted for age, sex, BMI and outdoor temperature with patients in the BAT^- group or those in tertile 1 (lowest BAT metabolic activity) as reference. The correlation of BAT activity with age and outside temperature was calculated with Pearson correlation coefficient after logarithmic transformation. The association of BAT activity with SAT area, VAT area, SAT to VAT ratio and other continuous clinical variables was calculated with linear regression after logarithmic transformation.

The association of BAT status and an expanded set of 511 ICD codes was assessed by univariable logistic regression to identify crude associations. ICD codes associated significantly with BAT were then analysed individually through multi-variable logistic regression analysis adjusting for age, sex, BMI, ambient temperature, self-reported race and ethnicity, smoking history, family history of cardiovascular disease, cancer site, cancer stage, cancer treatment and general groups of outpatient medications. For over-representation analysis, the 511 codes were grouped by organ system. Enrichment for each organ system category was calculated based on the proportion of BAT-associated ICD codes divided by the corresponding proportion among all diagnostic codes in the category set. Statistical significance of over-representation was assessed using Fisher's exact test and Benjamini–Hochberg FDR was used for multiple test adjustments.

Unpaired *t*-tests were used to compare laboratory values, imaging studies and clinical indices in patients in the BAT^+ versus BAT^- groups. Variance equality was assessed with an *F*-test. When variances were equal, standard *t*-tests assuming equal variances were used; otherwise, *t*-tests with unequal variance adjustments were applied. For adjusted analyses, GLMs were used to estimate least square means, adjusting for age, sex, BMI, self-reported race and ethnicity, ambient temperature, cancer site, cancer stage and cancer treatment. Post hoc pairwise comparisons were performed using Tukey's HSD method. Categorical variables were compared using Fisher's exact test.

Associations between BAT and individual medications were assessed through multi-variable logistic regression adjusted for age, sex, BMI, temperature, ethnicity, race, smoking history, family history of cardiovascular disease, cancer sites, cancer stage, cancer treatment and cardiovascular diagnoses. For in vitro and in vivo proof-of-concept experiments, group comparisons were conducted using unpaired *t*-tests. To account for multiple comparisons, *P* values were corrected using the Benjamini–Hochberg FDR method, and adjusted *P* values are reported as such where applicable. Metabolic cage data were analysed, and statistical significance was calculated either using two-way analysis of variance for hourly data or unpaired *t*-test for 24-h cumulative, light and dark cycle. All analyses were performed using SAS (v.9.4), R software (v.4.5.1) and GraphPad Prism (v.10.5.0). All reported *P* values are two-sided and statistical significance was defined as $\alpha < 0.05$.

Reporting summary

Further information on research design is available in the Nature Portfolio Reporting Summary linked to this article.

Data availability

Average monthly temperatures in Central Park were obtained from the National Weather Service website (https://www.weather.gov). Anonymized clinical data are available upon request to pcohen@rockefeller.edu, subject to an internal review by N.G.B., P.C., D.L. and H.S. to ensure that the participants' anonymity and confidentiality are protected and completion of a data sharing agreement, and in accordance with MSK Institutional Review Board and Institutional Guidelines. Requests for access to data will be responded to within 4 weeks. Source data are provided with this paper.

Code availability

The code that supports the findings of this study is available from MSK, but restrictions apply to its availability; it was used under licence for the current study, and so it is not publicly available. This code is however available from the authors upon reasonable request and with permission of MSK.

60. Lafontaine, D. et al. TriDFusion (3DF) image viewer. *EJNMMI Phys*. **9**, 72 https://doi.org/10.1186/s40658-022-00501-y (2022).
61. Wasserthal, J. et al. TotalSegmentator: robust segmentation of 104 anatomic structures in CT images. *Radiol Artif Intell* **5**, e230024 https://doi.org/10.1148/ryai.230024 (2023).
62. Chi, J. et al. Early postnatal interactions between beige adipocytes and sympathetic neurites regulate innervation of subcutaneous fat. *eLife* **10**, e64693 https://doi.org/10.7554/eLife.64693 (2021).
63. Chi, J. et al. Three-dimensional adipose tissue imaging reveals regional variation in beige fat biogenesis and PRDM16-dependent sympathetic neurite density. *Cell Metab.* **27**, 226–236 https://doi.org/10.1016/j.cmet.2017.12.011 (2018).
64. Moffat, J. et al. A lentiviral RNAi library for human and mouse genes applied to an arrayed viral high-content screen. *Cell* **124**, 1283–1298 https://doi.org/10.1016/j.cell.2006.01.040 (2006).
65. Tontonoz, P., Hu, E., Graves, R. A., Budavari, A. I. & Spiegelman, B. M. mPPAR gamma 2: tissue-specific regulator of an adipocyte enhancer. *Genes Dev.* **8**, 1224–1234 https://doi.org/10.1101/gad.8.10.1224 (1994).
66. Kim, J. B., Wright, H. M., Wright, M. & Spiegelman, B. M. ADD1/SREBP1 activates PPARgamma through the production of endogenous ligand. *Proc. Natl Acad. Sci. USA* **95**, 4333–4337 https://doi.org/10.1073/pnas.95.8.4333 (1998).
67. Pinol, R. A. et al. Brs3 neurons in the mouse dorsomedial hypothalamus regulate body temperature, energy expenditure, and heart rate, but not food intake. *Nat. Neurosci.* **21**, 1530–1540 https://doi.org/10.1038/s41593-018-0249-3 (2018).
68. Marks, A., Vianna, D. M. & Carrive, P. Nonshivering thermogenesis without interscapular brown adipose tissue involvement during conditioned fear in the rat. *Am. J. Physiol. Regul. Integr. Comp. Physiol.* **296**, R1239–R1247 https://doi.org/10.1152/ajpregu.90723.2008 (2009).
69. Li, M. Y. et al. Characterization of Ucp1-iCre knockin mice reveals the recombination activity in male germ cells. *Am. J. Physiol. Endocrinol. Metab.* **327**, E544–E551 https://doi.org/10.1152/ajpendo.00128.2024 (2024).
70. Sakamoto, K. et al. Overnutrition causes insulin resistance and metabolic disorder through increased sympathetic nervous system activity. *Cell Metab.* **37**, 121–137 https://doi.org/10.1016/j.cmet.2024.09.012 (2025).
71. Krisko, T. I. et al. Dissociation of adaptive thermogenesis from glucose homeostasis in microbiome-deficient mice. *Cell Metab.* **31**, 592–604 https://doi.org/10.1016/j.cmet.2020.01.012 (2020).
72. Weir, J. B. New methods for calculating metabolic rate with special reference to protein metabolism. *J. Physiol.* **109**, 1–9 https://doi.org/10.1113/jphysiol.1949.sp004363 (1949).

Acknowledgements We thank all members of the Laboratory of Molecular Metabolism and members of the Leducq CardioBAT Network for lively discussions and intellectual exchange. We thank P. Shobeiri for assistance with data management from the machine learning dataset and J. Schmeltz for extraction of data from the EHR.

Author contributions N.G.-B. and P.C. conceived and designed the study. N.G.-B. and J.A.B. extracted and structured the clinical data. N.G.-B., J.A.B., C.S.J. and T.L. conducted the statistical analyses. N.G.-B., J.A.B., N.K., M.K., L.R.P.d.C., K.P. and K.M. designed and performed experiments. N.G.-B. and R.S. designed, T.D.L. performed, and T.D.L. and R.S. analysed the metabolic cage experiments. D.L., S.C., G.B., H.S. and B.A.U. developed the machine learning approach to quantify BAT metabolic activity. N.G.-B., J.A.B., M.K., J.E.L., H.S. and P.C. provided technical and intellectual input. N.G.-B., J.E.L., H.S. and P.C. supervised study. N.G.-B. and P.C. wrote the original draft of the manuscript. All authors contributed to manuscript preparation.

Funding N.G.-B. and C.S.J. were supported in part by grant no. UL1 TR001866 from the National Center for Advancing Translational Sciences (NIH) Clinical and Translational Science Award programme. N.G.-B. was also supported by a Pilot Grant from the Rockefeller University Maurice R. and Corinne P. Greenberg Center for the Study of Inflammation, Microbiome and Metabolism, Burroughs Wellcome Weill Cornell Physician Scientist programme and the Career Award for Medical Scientists from the Burroughs Wellcome Fund. J.A.B. was supported in part by the Convocatoria de Apoyo para Movilidad Saliente from the Universidad Nacional de Colombia. N.K. was supported by a Medical Scientist Training Programme grant from the National Institute of General Medical Sciences of the NIH under award no. T32GM152349 to the Weill Cornell/Rockefeller/Sloan Kettering Tri-Institutional MD-PhD Programme. M.K. was supported through the German Research Foundation (Walter Benjamin KO 6368/1-1), the Charles H. Revson Foundation grant no. 23-22 and the Kellen Women's Entrepreneurship Fund with support from L. Wang. K.P. was supported by the Novo Nordisk Foundation Fellowship (NNF19OC0055021) and the Elizabeth Hall Janeway Award from the Kellen Women's Entrepreneurship Fund. K.M. was supported in part by a fellowship from the Boehringer Ingelheim Fonds. H.S., J.E.L. and D.L. were supported in part by the MSK support grant (P30 CA008748). P.C. was supported in part by DK139983 (NIH) and the Leducq Foundation.

Competing interests P.C. was on the Board of Directors of Amarin Corp. and is an advisor for Canary Cure Therapeutics, Hoxton Farms, Moonwalk Biosciences and Cellular Intelligence. None of these entities supported this research. The other authors declare no competing interests.

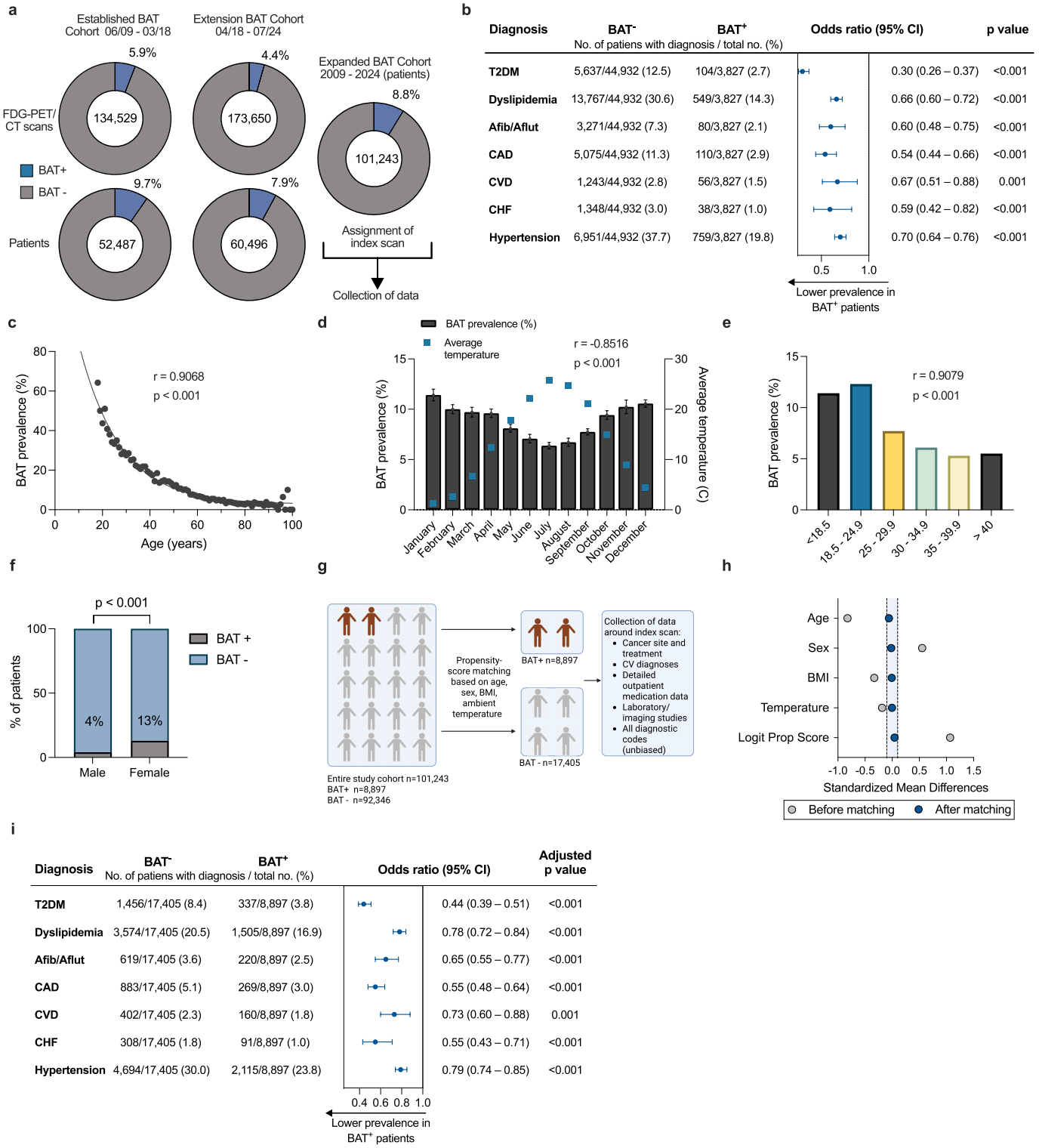
Additional information

Supplementary information The online version contains supplementary material available at https://doi.org/10.1038/s41586-026-11162-7.

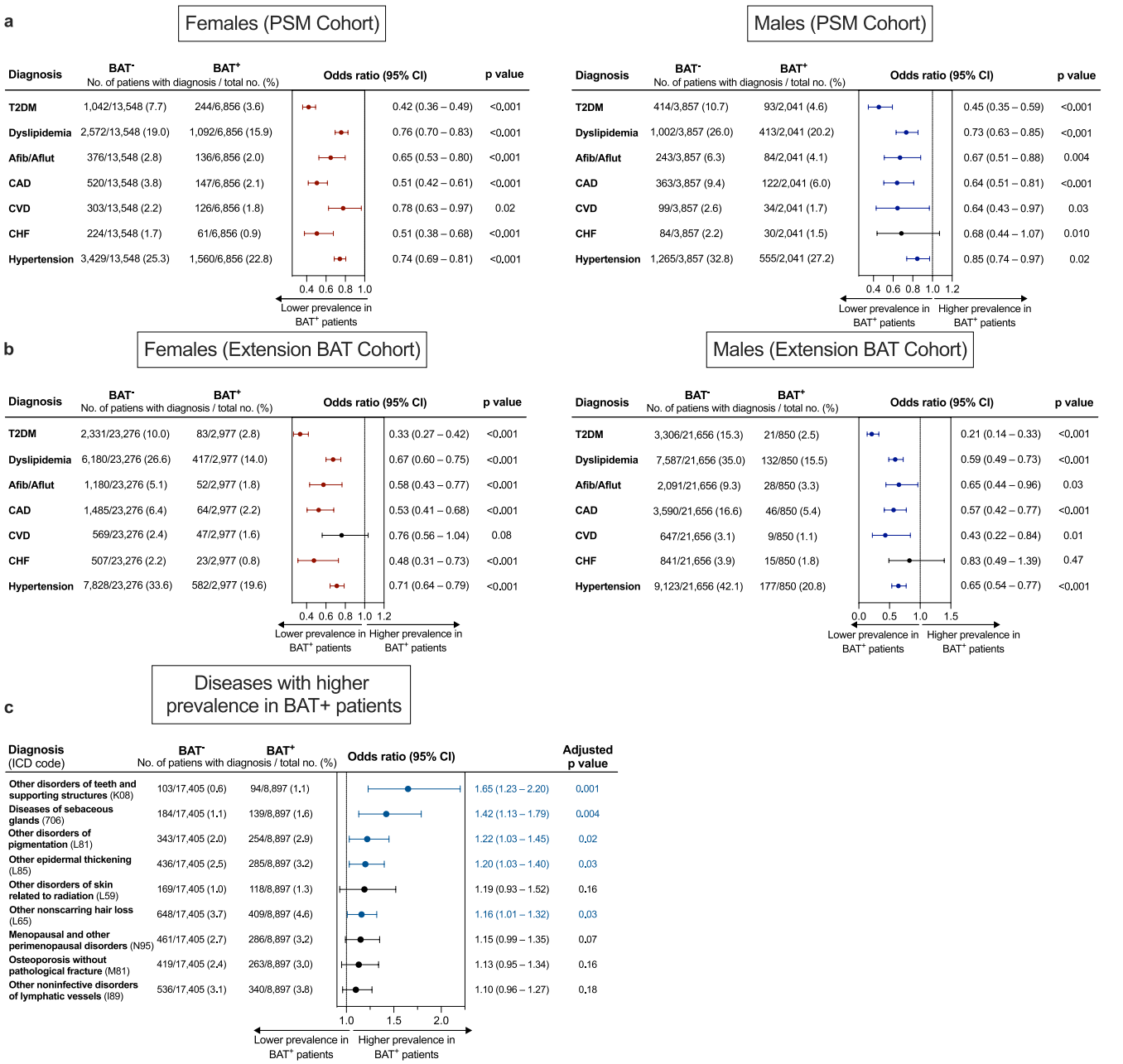
Correspondence and requests for materials should be addressed to Paul Cohen.

Peer review information *Nature* thanks Stephan Herzig, Kirsi Virtanen and the other, anonymous, reviewer(s) for their contribution to the peer review of this work. Peer reviewer reports are available.

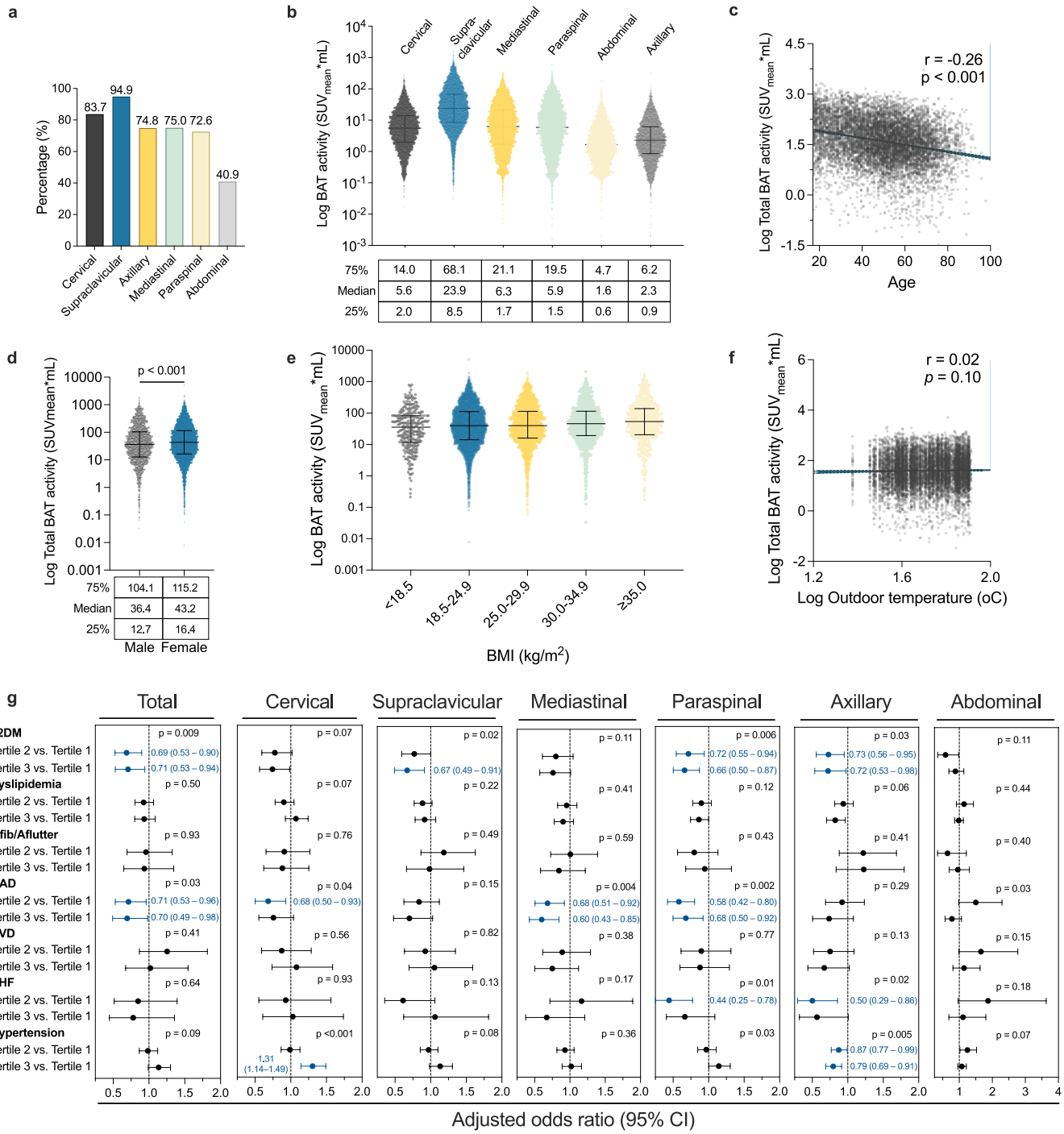
Reprints and permissions information is available at http://www.nature.com/reprints.



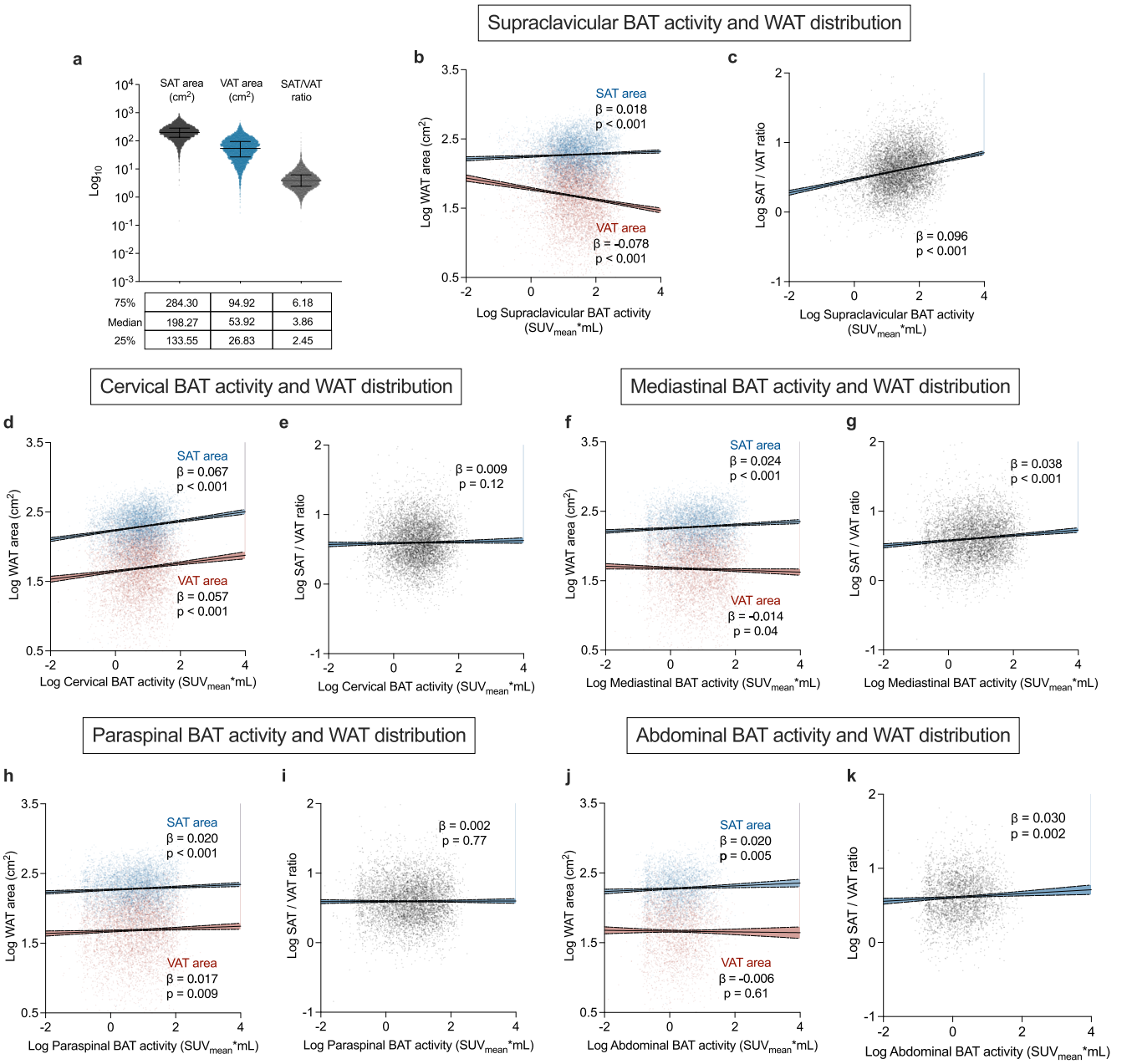
Extended Data Fig. 1 | Establishment of an Expanded BAT Cohort. a, Establishment of the Expanded BAT Cohort by merging the Established BAT Cohort and the Extension BAT Cohort. Pie charts depict prevalence of BAT + FDG-PET/CT scan reports and total BAT+ patients within the cohorts. b, Forest plot of odds ratios (OR) for associations between cardiovascular diagnoses and BAT status in patients unique to the Extension BAT Cohort. c, Correlation between BAT prevalence and age in the Expanded BAT cohort. d, BAT prevalence throughout the year based on FDG-PET scans from 06/09 through 05/24 and correlation with outside temperature. e, BAT prevalence across BMI categories. f, Prevalence of BAT stratified by sex. p value was calculated using chi-squared test. g, Establishment of a matched cohort via PSM based on age, sex, BMI and ambient temperature at the time of index scan. h, Comparison of standardized means before and after PSM. i, Forest plot of OR for associations between BAT status and cardiometabolic diseases in a propensity score matched (PSM) cohort. (b,i) Blue circles represents the estimated OR, and error bars denote the corresponding 95% confidence interval (CI). OR and p values obtained using multivariable logistic regression analysis after adjustment for age, sex, BMI, ambient temperature, self-reported race and ethnicity, smoking history, family history of cardiovascular disease, cancer site, cancer stage, cancer treatment, and general groups of outpatient medications. (c,d,e) p values obtained by Pearson's correlation coefficient. Panel **g** created in BioRender; Cohen, P. https://biorender.com/4nlc3zj (2026).



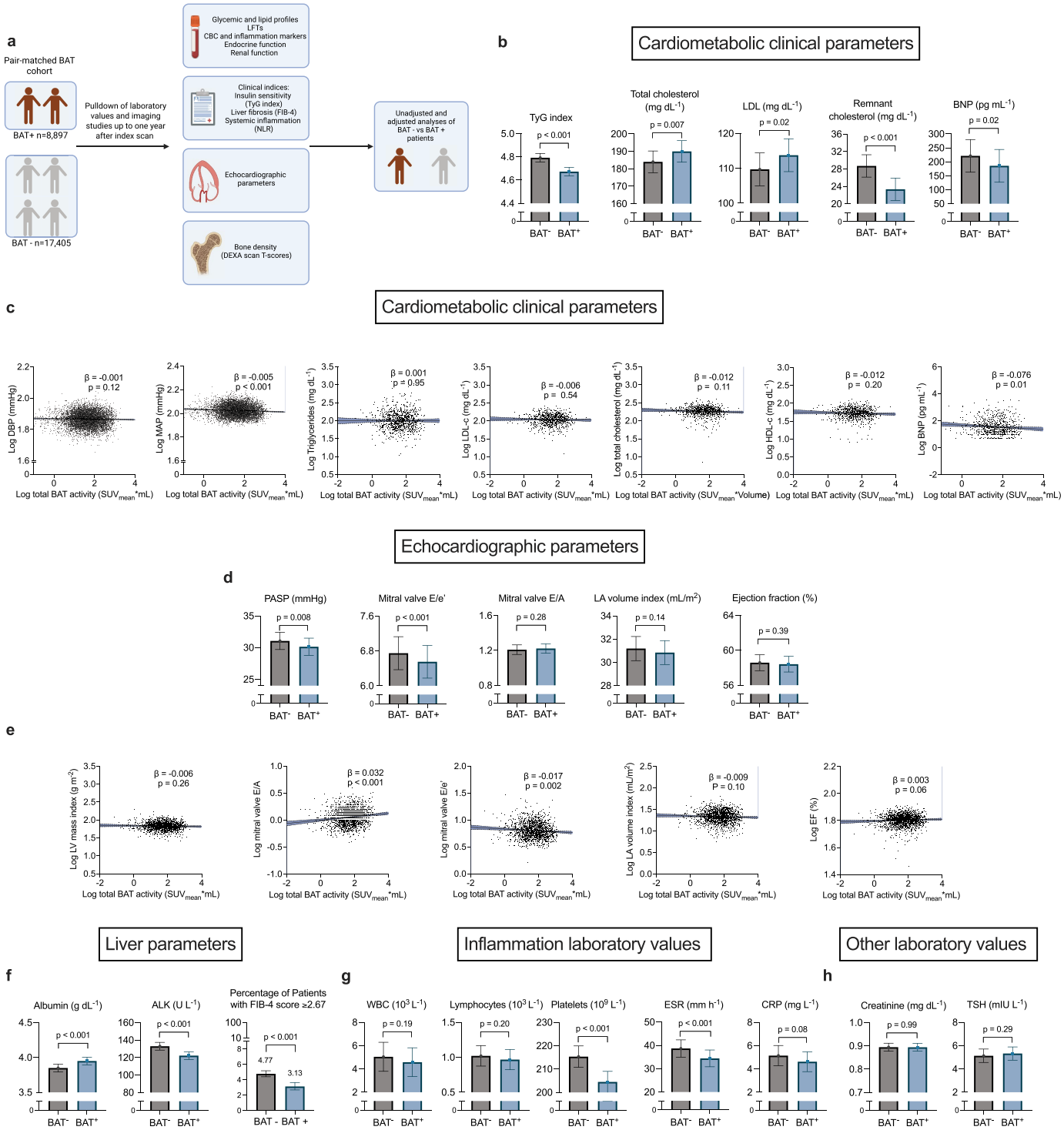
Extended Data Fig. 2 | Analyses stratified by sex and diseases with higher prevalence in BAT+ patients. a, Forest plots of odds ratios (OR) for associations between BAT status and cardiometabolic diseases in female patients only (left) (n = 20,404) and male patients only (right) (n = 5,898) from propensity score matched (PSM) cohort. b, Forest plots of OR for associations between BAT status and cardiometabolic diseases in female patients only (left) (n = 26,253) and male patients only (right) (n = 22,506) from the Extension BAT Cohort. c, Forest plot of OR for associations between diagnoses with higher prevalence in BAT positive patients (ranked by OR). (a-c), Circles (a,b red for females, blue for males) represent estimated OR, and error bars denote corresponding 95% confidence interval (CI). OR and p values were obtained using multivariable logistic regression analysis after adjustment for age, sex, BMI, ambient temperature, self-reported race and ethnicity, smoking history, family history of cardiovascular disease, cancer site, cancer stage, cancer treatment, and general groups of outpatient medications.



Extended Data Fig. 3 | Prevalence, metabolic activity of BAT depots, and association with cardiometabolic outcomes. a, Prevalence of BAT depots in BAT+ patients. b, Quantification of BAT metabolic activity with median, 25th and 75th percentiles in individual BAT depots in BAT+ patients. c, Scatter graph depicting correlation between total BAT metabolic activity and age. d, Quantification of BAT metabolic activity in male versus female patients. e, Quantification of BAT metabolic activity in each BMI category. f, Scatter graph depicting correlation between total BAT metabolic activity and outside temperature at the time of the scan. BAT metabolic activity was estimated by the product of SUV mean multiplied by BAT volume. (c,f) Correlations with age and outdoor temperature were calculated with Pearson correlation after logarithmic transformation in BAT+ patients with available measurements (n = 8,709). g, Forest plot of adjusted odds ratio (OR) for associations between total and depot-specific BAT activity stratified in tertiles (n = 2,903 per tertile) and cardiometabolic diseases using tertile 1 (lowest BAT metabolic activity) as a reference. Blue circles represent estimated OR, and error bars denote corresponding 95% confidence interval (CI). p values were obtained using a multivariable logistic regression analysis adjusted for age, sex, BMI and outdoor temperature at the time of the scan.

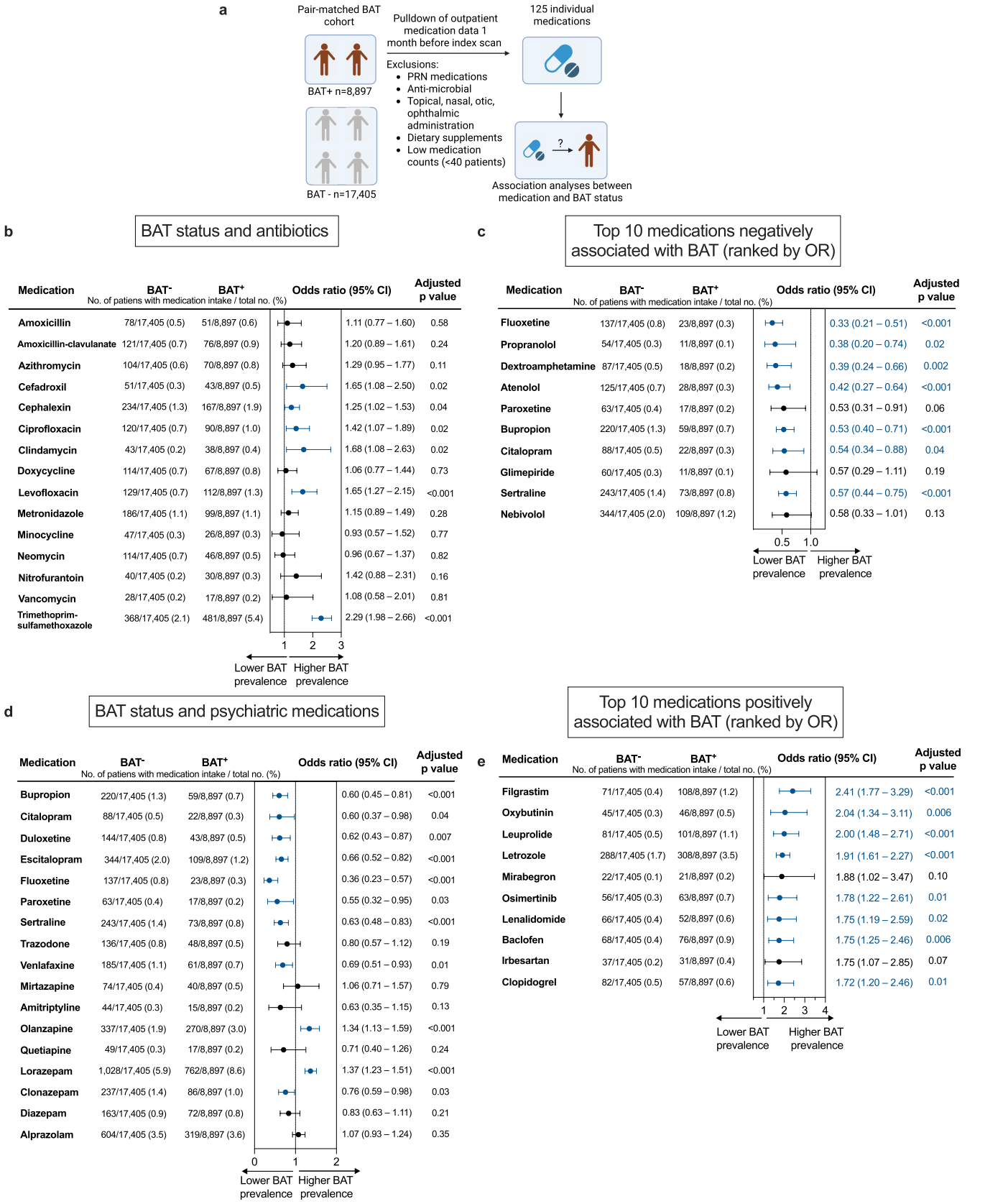


Extended Data Fig. 4 | WAT distribution phenotypes and associations with depot-specific BAT metabolic activity. a, Quantification of SAT area, VAT area, and SAT/VAT ratio with median, 25th and 75th percentiles in a cohort of 8,040 BAT+ patients. b-j, Scatter graphs depicting the association between b) supraclavicular (n = 7,628), d) cervical (n = 7,289), f) mediastinal (n = 6,045), h) paraspinal (n = 5,854), and j) abdominal (n = 3,285) BAT metabolic activity, with SAT and VAT area. c-h, Scatter graphs depicting associations between c) supraclavicular (n = 7,628), e) cervical (n = 7,289), g) mediastinal (n = 6,045), i) paraspinal (n = 5,854), and k) abdominal (n = 3,285) BAT metabolic activity with SAT/VAT ratio. Associations between depot-specific BAT metabolic activity and SAT area, VAT area, and SAT/VAT ratio were calculated using linear regression after logarithmic transformation. Regression coefficients (β) and corresponding p values are reported.



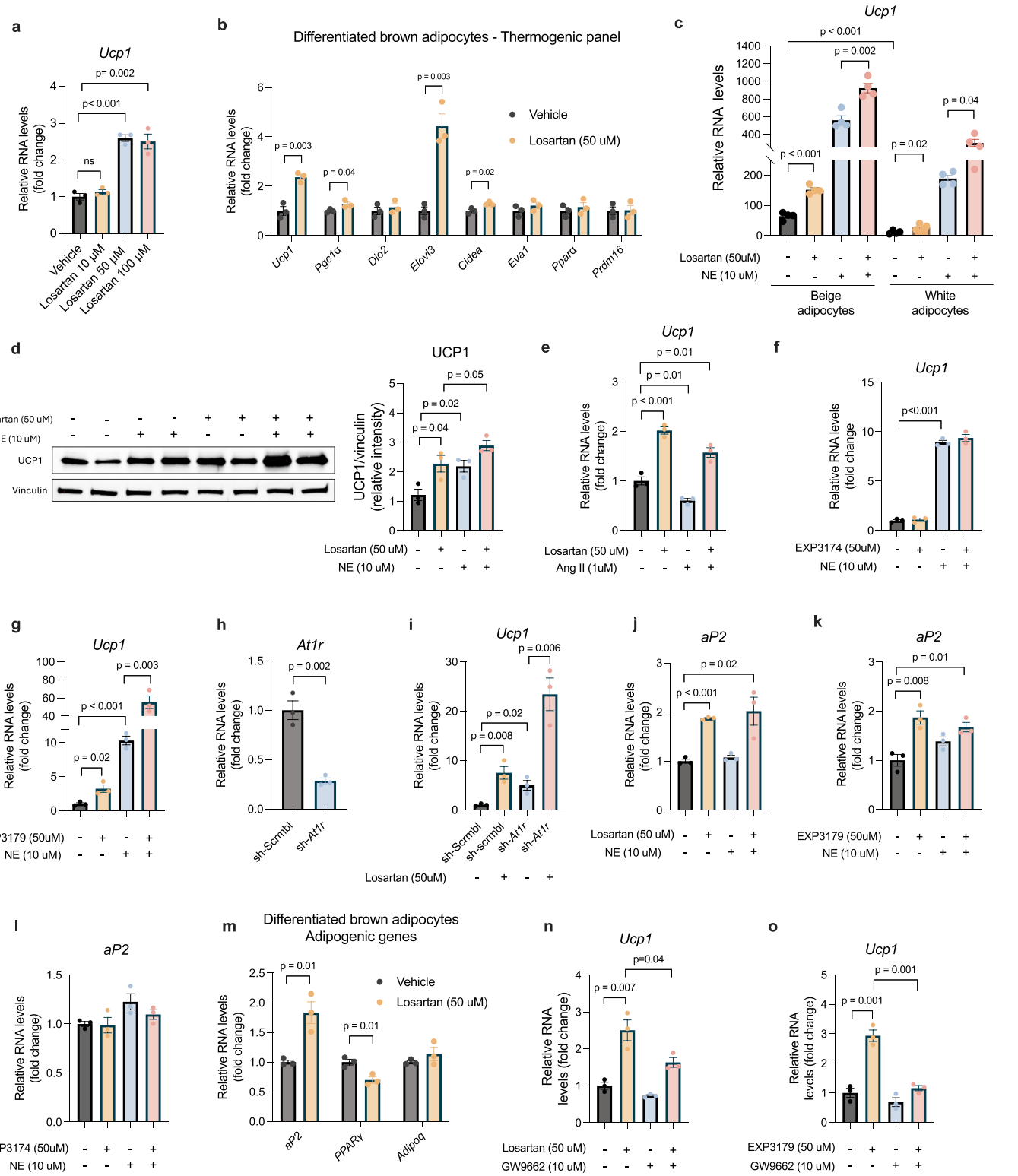
Extended Data Fig. 5 | See next page for caption.

Extended Data Fig. 5 | Association of BAT presence and metabolic activity with lab values and clinical parameters. a, Strategy to extract and analyze lab values, clinical indices, and imaging studies from patients in PSM cohort. b, Comparisons of metabolic lab values/indices in BAT negative (BAT-) versus BAT positive (BAT +) patients: triglyceride-to-glucose index (TyG; BAT- n = 1,996, BAT+ n = 995), total cholesterol (BAT- n = 1,746, BAT+ n = 900), low-density lipoprotein cholesterol (LDL-C; BAT- n = 1,568, BAT+ n = 818), remnant cholesterol (BAT- n = 1,558, BAT+ n = 815), and brain natriuretic peptide (BNP; BAT- n = 1,887, BAT+ n = 737). c, Scatter graphs depicting associations between total BAT metabolic activity and diastolic blood pressure (DBP; n = 6,482), mean arterial pressure (MAP; n = 6,482), triglycerides (n = 965), LDL-C (n = 794), total cholesterol (n = 872), HDL-C (n = 804), and BNP (n = 723). d, Comparisons of echocardiographic indices in BAT- versus BAT+ patients: pulmonary artery systolic pressure (PASP; BAT- n = 1,398, BAT+ n = 779), mitral valve E/e' ratio (BAT- n = 3,000, BAT+ n = 1,627), mitral valve E/A ratio (BAT- n = 3,052, BAT+ n = 1,645), left atrium volume index (LA volume index; BAT- n = 3,085, BAT+ n = 1,651), and ejection fraction (BAT- n = 3,234, BAT+ n = 1,715). e, Scatter graphs depicting associations between total BAT metabolic activity and: left ventricular mass index (LV mass index; n = 1,701), mitral valve E/A ratio (n = 1,616), mitral valve E/e' ratio (n = 1,597), LA volume index (n = 1,620), ejection fraction (EF; n = 1,683). f, Hepatic lab values/indices in BAT- versus BAT+ patients: albumin (BAT- n = 15,549, BAT+ n = 8,099), alkaline phosphatase (ALK; BAT- n = 15,512, BAT+ n = 8,082), and FIB-4 score (BAT- n = 11,624, BAT+ n = 5,327). g, Inflammatory lab values in BAT- versus BAT+ patients: white blood cells (WBC; BAT- n = 14,986, BAT+ n = 7,867), lymphocyte counts (BAT- n = 14,584, BAT+ n = 7,681), platelet counts (BAT- n = 14,985, BAT+ n = 7,867), erythrocyte sedimentation rate (ESR; BAT- n = 1,774, BAT+ n = 1,021), and C-reactive protein (CRP; BAT- N = 1,388, BAT+ n = 638). h, Other pertinent lab values in BAT- versus BAT+ patients: creatinine (BAT- n = 15,818, BAT+ n = 8,233) and thyroid stimulating hormone (TSH; BAT- n = 5,792, BAT+ n = 3,014). (b,d,f,g,h) Bar graphs depict mean values and error bars depict SEM. p values obtained using a general linear model (GLM) followed by post-hoc Tukey's HSD test to compare least square means, adjusted for age, sex, BMI, race, ethnicity, ambient temperature, cancer site and stage, cancer treatment, and outpatient medications. (f) p value for frequency of FIB-4 ≥ 2.67 between BAT+ and BAT- calculated using a Chi-square test. (c,e). Associations between BAT metabolic activity with continuous clinical variables were calculated using linear regression after logarithmic transformation. Regression coefficients (β) and corresponding p values are reported. Panel **a** created in BioRender; Gómez-Banoy, N. https://biorender.com/hfhen8d (2026).



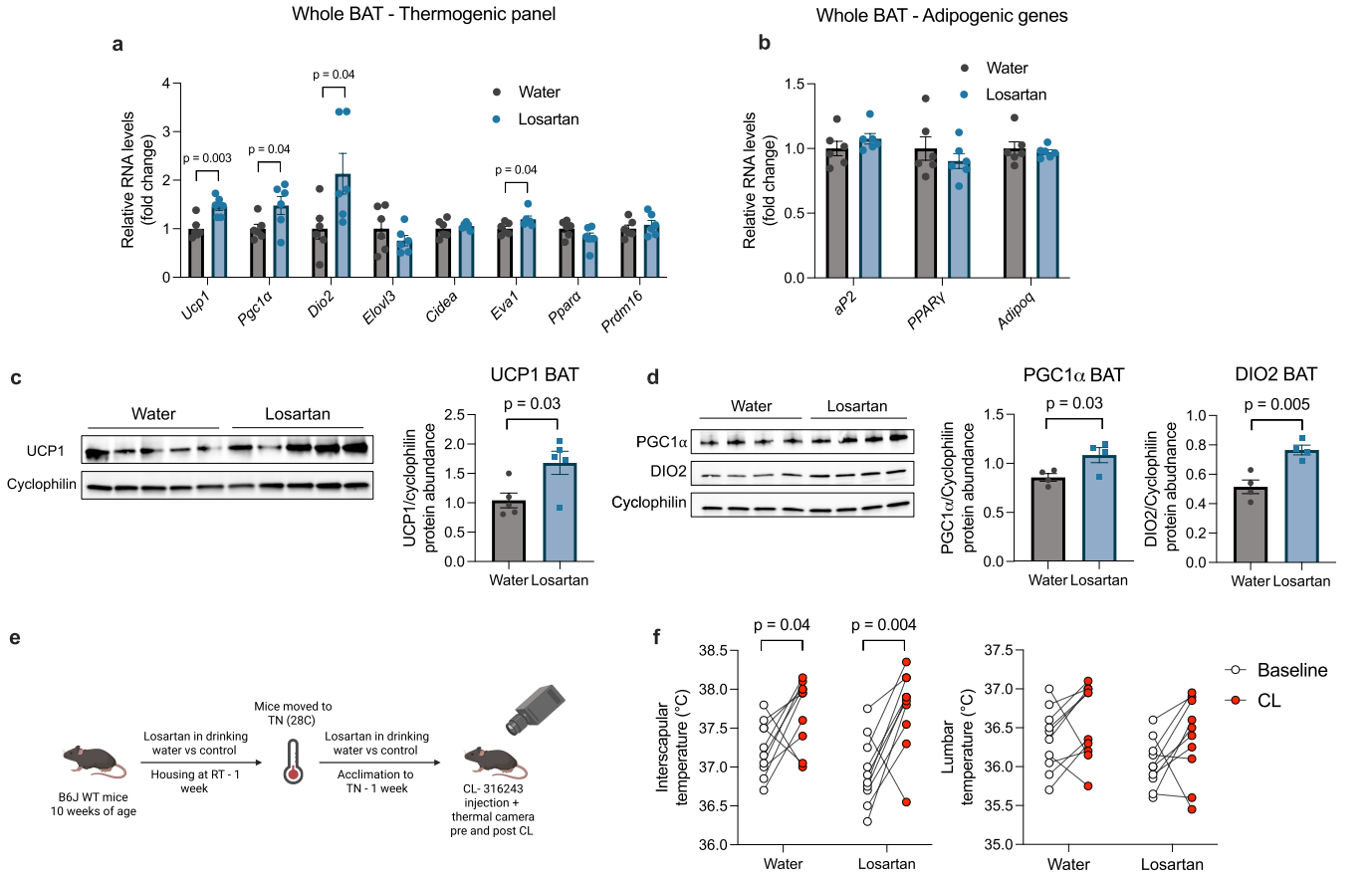
Extended Data Fig. 6 | See next page for caption.

Extended Data Fig. 6 | Associations of BAT with medications. a, Strategy for identification of ambulatory, chronic, individual medications in PSM cohort of 26,302 patients and proposed analyses. b, Forest plot of odds ratios (OR) for associations between antibiotic usage and BAT status in PSM cohort. c, Forest plot of ORs for top medications negatively associated with BAT presence. d, Forest plot of ORs for associations between antidepressant, anxiolytic, and antipsychotic usage and BAT status in PSM cohort. e, Forest plot of OR for top medications positively associated with BAT presence. (b-e), Blue circles represent estimated OR, and error bars denote corresponding 95% confidence interval (CI). ORs and p values estimated using multivariable logistic regression adjusting for age, sex, BMI, temperature, ethnicity, race, smoking history, family history of cardiovascular disease, cancer sites, cancer stage, cancer treatment, and cardiovascular diagnoses. For d, adjustment was additionally made for psychiatric diagnoses. Panel **a** created in BioRender; Cohen, P. https://biorender.com/0dgpm5s (2026).

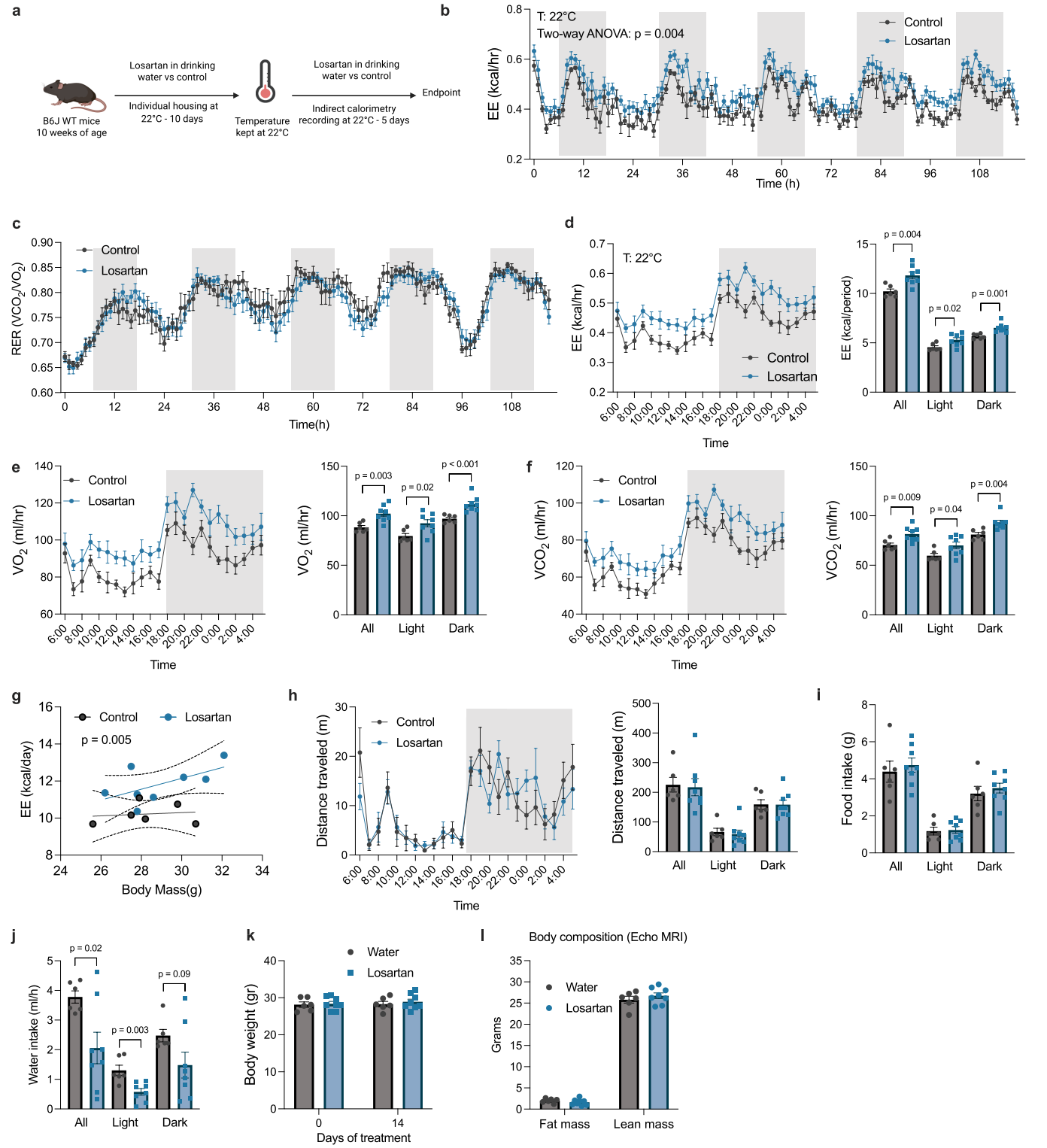


Extended Data Fig. 7 | See next page for caption.

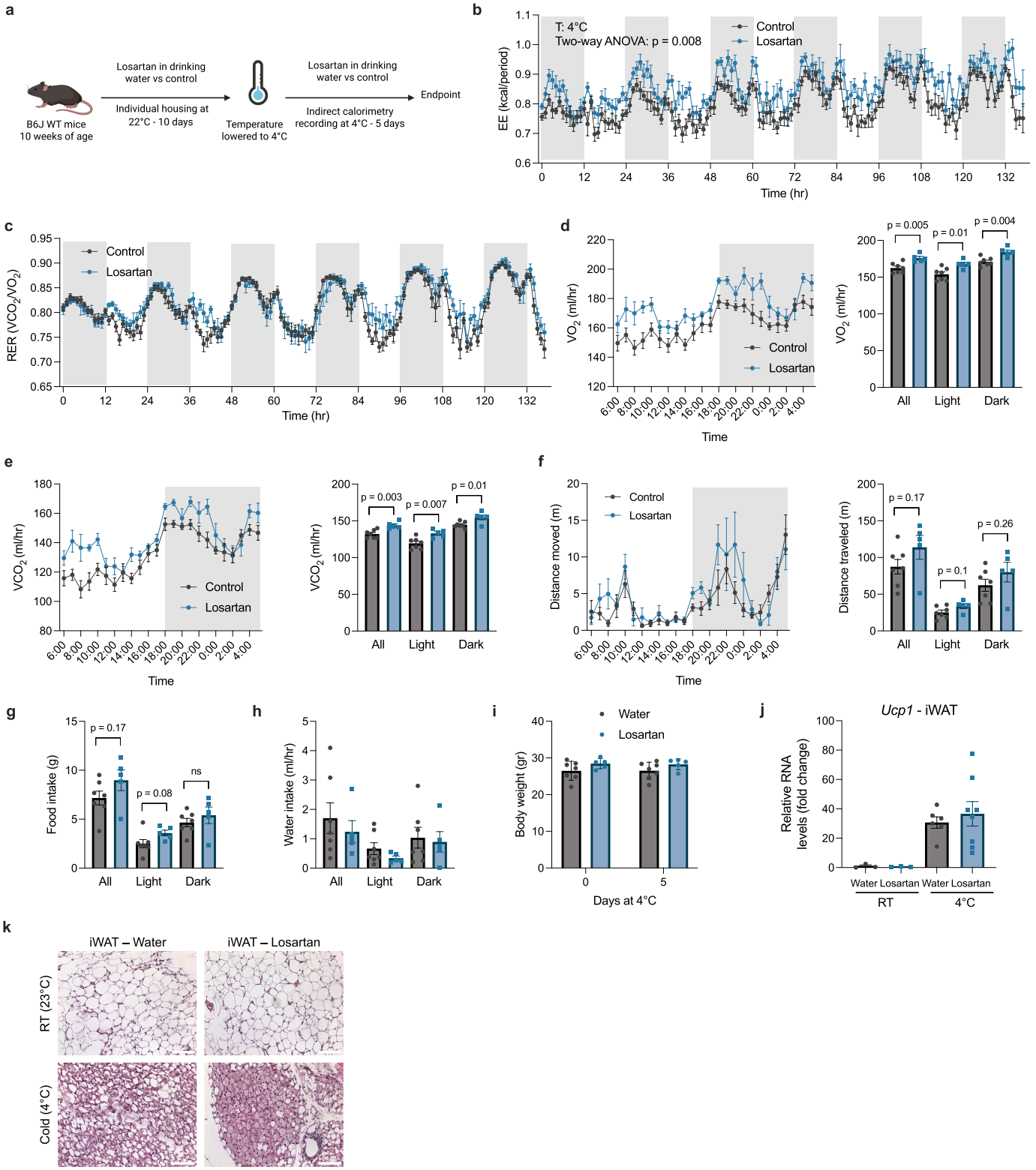
Extended Data Fig. 7 | Losartan promotes a PPARγ-dependent thermogenic gene program in brown adipocytes. a, *Ucp1* RNA levels in immortalized brown adipocytes treated with different doses of losartan or vehicle for 24 h. b, RNA levels of thermogenic genes in immortalized brown adipocytes after treatment with losartan or vehicle for 24 h. c, *Ucp1* RNA levels in mature white and beige adipocytes pre-treated with losartan or vehicle for 24 h and then stimulated with +/− norepinephrine (NE) for 6 h. d, Representative Western blot of UCP1 in primary brown adipocytes pre-treated with vehicle vs losartan for 48 h and then stimulated +/− norepinephrine (NE) for 16 h. Quantification of UCP1 protein relative to vinculin shown to the right. e, *Ucp1* RNA levels in brown adipocytes treated with vehicle, angiotensin II (1uM), losartan (50 uM), or co-treatment with angiotensin II and losartan for 24 h. f,g *Ucp1* RNA levels in immortalized brown adipocytes pre-treated with losartan metabolite (f) EXP3174 (50 uM) or (g) EXP3179 (50 uM) versus vehicle for 24 h and then stimulated +/− norepinephrine (NE) for 6 h. h,i Primary brown adipocytes transduced with lentivirus carrying an shRNA targeting *At1r* or scrambled (scrmbl) control. (h) *At1r* RNA levels quantified at baseline (i) *Ucp1* RNA levels quantified after treatment with losartan or vehicle for 24 h. j-l *aP2* RNA levels in immortalized brown adipocytes pre-treated with j) losartan, k) EXP3179, or l) EXP3174 versus vehicle for 24 h and then stimulated +/− norepinephrine (NE) for 6 h. m, RNA levels of adipogenesis genes in immortalized brown adipocytes after treatment with losartan or vehicle for 24 h. n,o *Ucp1* RNA levels in brown adipocytes pre-treated with GW9662 or vehicle for 24 h and then stimulated with n) losartan or o) EXP3179 + /- NE. All bar graphs in this figure depict mean +/− SEM. Each dot represents a biological replicate from one representative experiment. All experiments were repeated at least 2 times with similar results. p values obtained using unpaired, two tailed t-test.



Extended Data Fig. 8 | Effects of losartan treatment in vivo. a-c, 12-week-old C57Bl/6 J WT mice treated with losartan in their drinking water or via twice daily gavage (100 mg/kg/day) for 2 weeks at room temperature (RT). a,b, RNA levels of thermogenic and adipogenic genes in BAT extracted from losartan-treated mice (drinking water) versus controls (n = 6 mice in both groups). c, Representative Western blot of BAT UCP1 from losartan-treated mice versus controls. Quantification of UCP1 protein relative to cyclophilin is shown to the right (n = 5 mice per group). d, Representative Western blot of whole BAT PGC1α and DIO2 from losartan-treated mice versus controls. Quantification of PGC1α and DIO2 protein relative to cyclophilin shown to the right (n = 4 mice per group). a-d, Bar graphs depict mean +/− SEM. Each dot represents an individual mouse. p values obtained using unpaired, two tailed t-test. e, Schematic of experimental plan - B6J WT mice treated with losartan in their drinking water (100 mg/kg/day) or regular water at room temperature (RT), followed by acclimation to thermoneutrality (TN) for 1 week, then injected with CL-316243 at 1 mg/kg. Thermal camera images obtained at baseline and 2 h after CL injection. f, Quantification of interscapular temperature (left) and lumbar temperature (right) assessed by thermal camera at baseline and after CL injection (n = 10 mice per group, white circles represent temperature at baseline, red circles represent temperature post-CL in the same mouse). p values between baseline and post-CL values obtained using paired, two tailed t-tests for each mouse. Panel **e** created in BioRender; Gómez-Banoy, N. https://biorender.com/umtlkun (2026).



Extended Data Fig. 9 | Effects of losartan treatment on whole body energy expenditure at RT. a-k, 10-week-old B6J WT mice treated with losartan in their drinking water (100 mg/kg/day) or regular water for 10 days at room temperature (RT) followed by indirect calorimetry for 5 days in metabolic cages (Prometheon) (n = 8 in losartan group, n = 6 in controls). a, Schematic of experimental plan. b, Energy expenditure (EE) during 5 days at RT, circles represent mean EE per time point, error bars are SEM. c, Respiratory exchange ratio (RER) during 5 days at RT, circles represent mean EE per time point, error bars are SEM. d-f,h Left graph shows representative 24-h period (circles represent mean EE per time point, error bars are SEM) and right bar graph depicts mean +/− SEM of each parameter during whole 24-h period, dark phase and light phase. d, EE e, Oxygen consumption (VO_2). f, Carbon dioxide production (VCO_2). g, ANCOVA of EE vs body weight. p value obtained via simple linear regression for each group and comparing the slopes. h, Distance traveled. Bar graph depicts mean +/− SEM i, food intake during representative 24-h period. j, Bar graph depicts mean +/− SEM water intake during representative 24-h period. k, Bar graph depicts mean +/− SEM body weight of mice before and after treatment with losartan versus control. l, Bar graph depicts mean +/− SEM body composition as determined by echo MRI. All p values except (g) obtained using unpaired, two tailed t-test. Panel **a** created in BioRender; Gómez-Banoy, N. https://biorender.com/otenbly (2026).



Extended Data Fig. 10 | See next page for caption.

Extended Data Fig. 10 | Effects of losartan treatment on whole body energy expenditure upon cold exposure. a-i, 10-week-old B6J WT mice treated with losartan in their drinking water (100 mg/kg/day) or regular water for 10 days at room temperature (RT) and then challenged with cold temperature (4 °C) for 5 days in metabolic cages (Prometheon) (n = 5 mice in losartan group, n = 7 in water group). a, Schematic of experimental plan. b, Energy expenditure (EE) during 5 days of cold exposure, circles represent mean EE per time point, error bars are SEM. c, Respiratory exchange ratio (RER) during 5 days of cold exposure, circles represent mean EE per time point, error bars are SEM. d-f, Left graph shows representative 24-h period (circles represent mean EE per time point, error bars are SEM) and right bar graph depicts the mean +/− SEM of each parameter during the whole 24-h period, dark phase and light phase. d, Oxygen consumption (VO_2). e, Carbon dioxide production (VCO_2). f, Distance traveled. g, Bar graph depicts mean +/− SEM food intake during representative 24-h period. h, Bar graph depicts mean +/− SEM water intake during representative 24-h period. i, Bar graph depicts mean +/− SEM body weight before and after cold challenge in losartan-treated mice and controls. j, *Ucp1* RNA levels in whole inguinal white adipose tissue (iWAT) extracted from losartan-treated mice and controls at basal room temperature (RT) or at 4 °C for 5 days (RT; n = 4 mice per group. 4 °C; n = 8 losartan, n = 7 water). k, Representative images of H&E staining of iWAT derived from losartan-treated mice and controls at basal room temperature (RT) or at 4 °C for 5 days. Scale bar is at 10uM. All p values in this figure obtained using unpaired two tailed t-test. Panel **a** created in BioRender; Gómez-Banoy, N. https://biorender.com/krp9kbn (2026).

nature portfolio

Corresponding author(s): Paul Cohen, M.D., Ph.D.

Last updated by author(s): Jul 10, 2026

Reporting Summary

Nature Portfolio wishes to improve the reproducibility of the work that we publish. This form provides structure for consistency and transparency in reporting. For further information on Nature Portfolio policies, see our Editorial Policies and the Editorial Policy Checklist.

Statistics

For all statistical analyses, confirm that the following items are present in the figure legend, table legend, main text, or Methods section.

n/a	Confirmed	
☐	☒	The exact sample size (*n*) for each experimental group/condition, given as a discrete number and unit of measurement
☐	☒	A statement on whether measurements were taken from distinct samples or whether the same sample was measured repeatedly
☐	☒	The statistical test(s) used AND whether they are one- or two-sided *Only common tests should be described solely by name; describe more complex techniques in the Methods section.*
☐	☒	A description of all covariates tested
☐	☒	A description of any assumptions or corrections, such as tests of normality and adjustment for multiple comparisons
☐	☒	A full description of the statistical parameters including central tendency (e.g. means) or other basic estimates (e.g. regression coefficient) AND variation (e.g. standard deviation) or associated estimates of uncertainty (e.g. confidence intervals)
☐	☒	For null hypothesis testing, the test statistic (e.g. *F*, *t*, *r*) with confidence intervals, effect sizes, degrees of freedom and *P* value noted *Give P values as exact values whenever suitable.*
☒	☐	For Bayesian analysis, information on the choice of priors and Markov chain Monte Carlo settings
☐	☒	For hierarchical and complex designs, identification of the appropriate level for tests and full reporting of outcomes
☐	☒	Estimates of effect sizes (e.g. Cohen's *d*, Pearson's *r*), indicating how they were calculated

Our web collection on statistics for biologists contains articles on many of the points above.

Software and code

Policy information about availability of computer code

Data collection	Data was organized using R software (version 4.5.1)
Data analysis	All analyses were performed using SAS (version 9.4), R software (version 4.5.1), and GraphPad Prism (version 10.5.0).

For manuscripts utilizing custom algorithms or software that are central to the research but not yet described in published literature, software must be made available to editors and reviewers. We strongly encourage code deposition in a community repository (e.g. GitHub). See the Nature Portfolio guidelines for submitting code & software for further information.

Data

Policy information about availability of data

All manuscripts must include a data availability statement. This statement should provide the following information, where applicable:

- Accession codes, unique identifiers, or web links for publicly available datasets
- A description of any restrictions on data availability
- For clinical datasets or third party data, please ensure that the statement adheres to our policy

Average monthly temperatures in Central Park were obtained from the National Weather Service website. Anonymized clinical data are available upon request, subject to an internal review by N.G.B., P.C., D.L. and H.S. to ensure that the participants' anonymity and confidentiality are protected and completion of a data sharing agreement, and in accordance with The Rockefeller University and Memorial Sloan Kettering Cancer Center Institutional Review Board and Institutional Guidelines.

Research involving human participants, their data, or biological material

Policy information about studies with human participants or human data. See also policy information about sex, gender (identity/presentation), and sexual orientation and race, ethnicity and racism.

Reporting on sex and gender	Sex was determined based on self-report, and extracted from the institutional EHR.
Reporting on race, ethnicity, or other socially relevant groupings	Race/ethnicity were determined based on self-report. Race/ethnicity categories are presented as reported in the institutional EHR.
Population characteristics	Patients aged 18 or above with available FDG-PET/CT scan data from June 2009 to July 2024 at Memorial Sloan Kettering Cancer Center
Recruitment	Given the retrospective nature of the study no active recruitment was needed.
Ethics oversight	This retrospective case–control study followed institutional guidelines and was approved by the Institutional Review Boards of The Rockefeller University and Memorial Sloan Kettering Cancer Center (MSK). Due to its retrospective nature, requirement for informed consent was waived.

Note that full information on the approval of the study protocol must also be provided in the manuscript.

Field-specific reporting

Please select the one below that is the best fit for your research. If you are not sure, read the appropriate sections before making your selection.

☒ Life sciences ☐ Behavioural & social sciences ☐ Ecological, evolutionary & environmental sciences

For a reference copy of the document with all sections, see nature.com/documents/nr-reporting-summary-flat.pdf

Life sciences study design

All studies must disclose on these points even when the disclosure is negative.

Sample size	No sample calculation was performed. Sample size was chosen based on independent preliminary studies
Data exclusions	On indirect calorimetry experiments done on WT mice treated with losartan vs control at 4°Cl, 3 mice were excluded due to technical issues with the metabolic cage airflow during the course of the experiment, leading to problematic O2 and CO2 recordings. This issues were independently confirmed by the company (Sable). On the indirect calorimetry experiment done on WT mice treated with losartan vs control at room temperature, 1 mouse was excluded due to outlier measurements in all parameters. ROUT testing confirmed this mouse was an outlier based on statistical testing.
Replication	Experimental findings were verified by biological replicates and by validation of at least two independent experiments.
Randomization	Samples/animals were randomly assigned when possible to control vs treatment groups.
Blinding	Experimenters were blinded by group allocation as much as possible when performing standardized sample processing.

Reporting for specific materials, systems and methods

We require information from authors about some types of materials, experimental systems and methods used in many studies. Here, indicate whether each material, system or method listed is relevant to your study. If you are not sure if a list item applies to your research, read the appropriate section before selecting a response.

Materials & experimental systems

n/a	Involved in the study
☐	☒ Antibodies
☐	☒ Eukaryotic cell lines
☒	☐ Palaeontology and archaeology
☐	☒ Animals and other organisms
☐	☒ Clinical data
☒	☐ Dual use research of concern
☒	☐ Plants

Methods

n/a	Involved in the study
☒	☐ ChIP-seq
☒	☐ Flow cytometry
☒	☐ MRI-based neuroimaging

Antibodies

Antibodies used	anti-UCP1 (1:1000, Abcam Ab209483), anti-Cyclophilin B (1:1000, Abcam Ab 16045, anti-vinculin (1:1000, #4650)
Validation	Antibodies were validated per manufacturers website https://www.abcam.com/en-us/products/primary-antibodies/ucp1-antibody-epr20381-ab209483, https://www.cellsignal.com/products/primary-antibodies/vinculin-antibody/4650?srsltid=AfmBOop0g0mAMI46LmbFaW7LpCqymTJelV7a53f7rcSar4-S643WfaDE, https://www.abcam.com/en-us/products/primary-antibodies/cyclophilin-b-antibody-loading-control-ab16045

Eukaryotic cell lines

Policy information about cell lines and Sex and Gender in Research

Cell line source(s)	Immortalized brown adipocytes were generated in the Cohen Lab. HEK293T cells used for lentiviral production were obtained from ATCC.
Authentication	Immortalized brown adipocytes were authenticated based on increased respiration and Ucp1 expression in response to norepinephrine.
Mycoplasma contamination	All cells were tested for mycoplasma contamination via PCR via and were negative.
Commonly misidentified lines (See ICLAC register)	N/A

Animals and other research organisms

Policy information about studies involving animals; ARRIVE guidelines recommended for reporting animal research, and Sex and Gender in Research

Laboratory animals	C57Bl6/J wild-type (WT) at 12 weeks of age were used in this study.
Wild animals	N/A
Reporting on sex	Only male mice were used in this study.
Field-collected samples	N/A
Ethics oversight	Animal care and experimentation were performed according to procedures approved by the Institutional Animal Care and Use Committee at the Rockefeller University.

Note that full information on the approval of the study protocol must also be provided in the manuscript.

Clinical data

Policy information about clinical studies

All manuscripts should comply with the ICMJE guidelines for publication of clinical research and a completed CONSORT checklist must be included with all submissions.

Clinical trial registration	N/A
Study protocol	MSK IRB 17-581
Data collection	We collected pertinent clinical data for each patient as previously described in Becher et al, Nat Med, 2021. In brief, for cancer site, we included the specific cancer diagnostic code (ICD-0) listed closest to the index scan date (Supplementary Table 1). Data referring to cancer treatment were collected if administered within 90 days before the index scan and classified as previously4 (Supplementary Table 2). Pertinent ICD-9 and ICD-10 codes corresponding to cardiometabolic diseases (Supplementary Table 7), and all other codes were extracted up to 1 year after the index scan in patients from our PSM cohort. Codes were selected to represent non-pediatric, non-obstetric, adult disorders as explained below. For laboratory values, clinical indices, and imaging studies, we extracted available data up to 1 year after the index scan in our PSM cohort. Analyses were performed in BAT+ and BAT- patients with available values. To identify individual pharmacological agents associated with BAT presence, we extracted medications in the home medication list and/or medications with an active pharmacy prescription in the EHR from each patient belonging to our PSM cohort. We included only medications listed up one month before the index scan for each patient. We excluded pharmacological agents with unlikely systemic effects, such as those with topical, ophthalmic, nasal, and otic administration. Antimicrobials were excluded since they are generally prescribed in short courses. Medications classified as “as needed” (PRN) and herbal supplements were excluded. Medications with low frequency counts (present in less than 40 patients) were excluded. A final list of medications included in the analyses can be found in Supplementary Table 8. These medications were also grouped by general categories as described in Supplementary Table 8. Selection of diagnostic codes for unbiased associations with BAT To explore unbiased associations between BAT and other diseases, we extracted from the electronic health records (EHR) diagnostic codes (ICD-9 and ICD-10) listed up to 1 year after the index scan from patients belonging to our propensity score-matched (PSM)

cohort. To select the codes for extraction, we grouped ICD-9 and ICD-10 codes based on their 3 first letters/digits. ICD-10 codes belonging to general groupings: A, B, C, D, E, F, G, H, I, J, K, L, M, N, R were included since they group the medical pathologies most likely to be found in a non-pediatric, non-obstetric, adult cancer population. A similar rationale was used for the selection of ICD-9 codes. A total of 1,157 ICD-10 codes and 626 ICD-9 codes were queried for extraction from the EHR.
After the code extraction was performed, to avoid redundancy, we merged ICD-9 codes with their corresponding ICD-10 codes based on a manual review of each code. The nomenclature of the ICD-10 code was maintained for downstream analysis in cases where an ICD-10 and ICD-9 code were merged. ICD-9 codes that did not have a corresponding ICD-10 code were maintained with their nomenclature. This left us with a total of 1,209 codes between individual ICD-9 and merged ICD-9/ICD-10 codes.
To further filter diagnostic codes for analyses, we excluded codes with low frequencies (present in less than 40 patients) and those referring to a cancer diagnosis (Supplementary Table 1) given all patients had a cancer site assigned already. This left us with a final list of 511 diagnostic codes. Given the large number of codes, we initially performed a screening analysis utilizing a univariable logistic regression analysis to identify unadjusted associations of the 511 with the presence of BAT. 104 codes were significantly associated with BAT status in this analysis. Subsequently, we analyzed each of these 104 codes using a multivariable regression analysis to assess their individual association with BAT, while controlling for age, sex, BMI, ambient temperature, self-reported race and ethnicity, smoking history, family history of cardiovascular disease, cancer site, cancer stage, cancer treatment, and general groups of outpatient medications (Extended Data Fig. 5a).

Outcomes

The association between BAT and age/BMI/temperature was assessed by a Pearson's correlation coefficient. Prevalence of BAT in men and women was compared using a chi-squared test.
To assess whether BAT status was a predictor of cardiometabolic diseases in the PSM cohort, we used multivariable logistic regression adjusting for age, sex, BMI, ambient temperature, self-reported race and ethnicity, smoking history, family history of cardiovascular disease, cancer site, cancer stage, cancer treatment, and general groups of outpatient medications. BAT metabolic activity (total and depot-specific) was calculated as the product of Standardized Uptake Value (SUV) mean and BAT volume (mL) and stratified into tertiles. The association of BAT activity with cardiometabolic diseases was assessed via a multivariable logistic regression adjusted age, sex, BMI, and outdoor temperature with BAT- patients or BAT patients in tertile 1 (lowest BAT metabolic activity) as reference. The correlation of BAT activity with age and outside temperature was calculated with Pearson correlation coefficient after logarithmic transformation. The association of BAT activity with SAT area, VAT area, SAT/VAT ratio, and other clinical continuous variables was calculated with linear regression after logarithmic transformation.
The association of BAT status and an expanded set of 511 ICD codes was assessed via univariable logistic regression to identify crude associations. ICD codes significantly associated with BAT were then individually analyzed through multivariable logistic regression analysis adjusting for age, sex, BMI, ambient temperature, self-reported race and ethnicity, smoking history, family history of cardiovascular disease, cancer site, cancer stage, cancer treatment, and general groups of outpatient medications. For overrepresentation analysis (ORA), the 511 codes were grouped by organ system.
Unpaired t-tests were used to compare lab values, imaging studies, and clinical indices in BAT+ vs BAT- patients. Variance equality was assessed via an F-test. When variances were equal, standard t-tests assuming equal variances were used; otherwise, t-tests with unequal variance adjustments were applied. For adjusted analyses, general linear models (GLMs) were used to estimate least square means, adjusting for age, sex, BMI, self-reported race and ethnicity, ambient temperature, cancer site, cancer stage, and cancer treatment. Post-hoc pairwise comparisons were performed using Tukey's HSD method. Categorical variables were compared using Fisher's exact test.
Associations between BAT and individual medications were assessed through multivariable logistic regression adjusted for age, sex, BMI, temperature, ethnicity, race, smoking history, family history of cardiovascular disease, cancer sites, cancer stage, cancer treatment, and cardiovascular diagnoses. For in vitro and in vivo proof-of-concept experiments, group comparisons were conducted using unpaired t-tests. To account for multiple comparisons, P values were corrected using the Benjamini-Hochberg false discovery rate (FDR) method, and adjusted P values are reported as such where applicable. Metabolic cage data were analyzed, and statistical significance was calculated either using 2-way ANOVA for hourly data or unpaired t-test for 24hr cumulative, light, and dark cycle.All analyses were performed using SAS (version 9.4), R software (version 4.5.1), and GraphPad Prism (version 10.5.0). All reported P values are two-sided, and statistical significance was defined as $\alpha < 0.05$.

Plants

Seed stocks

Report on the source of all seed stocks or other plant material used. If applicable, state the seed stock centre and catalogue number. If plant specimens were collected from the field, describe the collection location, date and sampling procedures.

Novel plant genotypes

Describe the methods by which all novel plant genotypes were produced. This includes those generated by transgenic approaches, gene editing, chemical/radiation-based mutagenesis and hybridization. For transgenic lines, describe the transformation method, the number of independent lines analyzed and the generation upon which experiments were performed. For gene-edited lines, describe the editor used, the endogenous sequence targeted for editing, the targeting guide RNA sequence (if applicable) and how the editor was applied.

Authentication

Describe any authentication procedures for each seed stock used or novel genotype generated. Describe any experiments used to assess the effect of a mutation and, where applicable, how potential secondary effects (e.g. second site T-DNA insertions, mosiacism, off-target gene editing) were examined.